



university of  
 groningen

faculty of mathematics  
 and natural sciences

kapteyn astronomical  
 institute

---

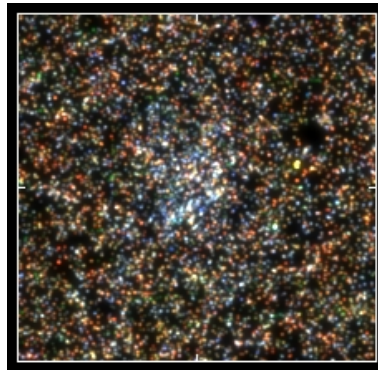
---

# Zinc and yttrium

Understanding the chemical evolution of the Boötes I dwarf spheroidal

---

---



*Author:*  
 Sietske J. D. Bouma

*Supervisors:*  
 Prof. dr. Eline Tolstoy  
 Dr. Ása Skúladóttir

## Abstract

Dwarf galaxies are small systems with relatively simple histories. This makes them interesting objects to study a “simple” chemical evolution history. Boötes I belongs to the faintest subclass of dwarf galaxies: ultra-faint dwarf spheroidals, which have very low surface brightness and are dark matter dominated.

High-resolution spectra from VLT/UVES for 8 RGB stars, with  $-3.7 < [\text{Fe}/\text{H}] < -2.1$ , in Boötes I were used in this project to find the abundances of Zn, Y and Zr and to re-measure several other elements to compare to an earlier analysis by Gilmore et al. (2013). Abundances are measured by using synthetic spectra which are made by using MARCS stellar atmosphere models and Turbospec. From these abundances, similarities and differences between the chemical evolution history of Boötes I and the more massive dSph Sculptor can be investigated. A comparison to abundances in Milky Way halo stars can also be made. The abundances are also compared to the yields of zero-metallicity SNe to estimate the properties of the first SNe that have enriched Boötes I.

In Boötes I,  $[\text{Y}/\text{Fe}]$  is constant, this is also seen in the Milky Way halo and in Sculptor.  $[\text{Zn}/\text{Fe}]$  appears to be constant in Boötes I, just as in the halo. This is different from the decrease in  $[\text{Zn}/\text{Fe}]$  with  $[\text{Fe}/\text{H}]$  seen in Sculptor. Boötes I seems to be enriched by zero-metallicity SNe of low mass ( $M < 28 M_{\odot}$ ), while the Milky Way halo, which is more massive, is enriched by more massive primordial SNe. Sculptor is intermediate between the halo and Boötes I.

# Contents

<b>1</b>	<b>Introduction</b>	<b>4</b>
1.1	Different formation scenarios . . . . .	4
1.2	Chemical evolution . . . . .	5
1.3	The Boötes I dwarf galaxy . . . . .	5
1.4	Outline . . . . .	7
<b>2</b>	<b>Spectroscopic data of Boötes</b>	<b>8</b>
2.1	The FLAMES-UVES spectrograph . . . . .	8
2.2	Data . . . . .	9
2.3	Zinc, yttrium and zirconium . . . . .	9
<b>3</b>	<b>Synthetic spectra</b>	<b>11</b>
3.1	MARCS models . . . . .	12
3.2	Turbospec . . . . .	12
<b>4</b>	<b>Data reduction</b>	<b>14</b>
4.1	The FLAMES-UVES pipeline . . . . .	14
4.2	Sky subtraction . . . . .	17
4.3	Coadding and normalizing spectra . . . . .	17
<b>5</b>	<b>Results</b>	<b>20</b>
5.1	Iron . . . . .	20
5.2	Magnesium . . . . .	24
5.3	Barium . . . . .	26
5.4	Zinc . . . . .	27
5.5	Strontium . . . . .	27
5.6	Yttrium . . . . .	28
5.7	Zirconium . . . . .	28
5.8	Errors . . . . .	29
<b>6</b>	<b>Abundance patterns of stars in different environments</b>	<b>31</b>
6.1	Interpretation of elemental abundance ratios . . . . .	31
6.1.1	Mg . . . . .	31
6.1.2	Ba . . . . .	32
6.1.3	Zn . . . . .	33
6.1.4	Y . . . . .	34
6.1.5	Zr . . . . .	36
6.2	Averaged abundance patterns . . . . .	37
6.2.1	Global abundance patterns . . . . .	37
6.2.2	Looking for hints of inhomogeneous mixing . . . . .	38
6.2.3	Abundance patterns and star formation histories . . . . .	41
6.2.4	Comparison to CEMP-no stars . . . . .	41
<b>7</b>	<b>Primordial SNe in Boötes</b>	<b>43</b>
7.1	Starfit . . . . .	43
7.2	Results . . . . .	43
7.2.1	Starfit for Boötes . . . . .	44
7.2.2	Starfit for the Milky Way halo . . . . .	45
7.2.3	Starfit for Sculptor . . . . .	46
7.2.4	Starfit for single stars . . . . .	46
<b>8</b>	<b>Discussion</b>	<b>48</b>
8.1	Zn, Y and Zr . . . . .	48
8.2	What are the properties of primordial SNe in Boötes? . . . . .	48
8.3	Is there a difference between chemical evolution properties in different environments? . . . . .	49

<b>9 Conclusion</b>	<b>50</b>
<b>10 Acknowledgements</b>	<b>51</b>
<b>References</b>	<b>52</b>
<b>Appendices</b>	<b>54</b>
<b>A Linelist</b>	<b>54</b>

# 1 Introduction

There are no laboratories in which we can set up experiments with controlled conditions in astronomy, which makes it quite difficult to interpret what is observed, but we can search for environments that are self-contained, such as dwarf galaxies. These small systems that are in an orbit around a larger galaxy such as our Milky Way have less stars, making it easier to get statistically significant results and have a simple stellar population that is not likely to be affected by merging events. They can teach us more about chemical evolution and about the first galaxies and stars that formed in the Universe. Since it is possible that the Milky Way halo formed from these systems, they can also be used to unravel part of the story of the formation and evolution of the Milky Way. Even though they are much larger than the average laboratory, dwarf galaxies are still small enough that we can hope to understand the complete path of chemical evolution that they have followed.

Examples of nearby, fairly large and luminous dwarf galaxies are the Small Magellanic Cloud and the Large Magellanic Cloud, both of them have been known since prehistoric times, since they can be observed by eye. Most dwarf galaxies are much fainter, hence the discovery of other dwarfs took some time. From analysing the large amount of data from the Sloan Digital Sky Survey (SDSS) several ultra-faint dwarf galaxies have been found, Boötes I being one of them (Belokurov et al., 2006). Boötes I is an ultra-faint dwarf spheroidal (dSph) galaxy. These ultra-faint dwarf galaxies have particularly low surface-brightness and are a faint subclass of dwarf galaxy. Dwarf galaxies can also have an elliptical or irregular shape and they can have a range of luminosities.

All galaxies, including dwarf galaxies, are divided into several types according to mass and luminosity. Properties like metallicity and surface brightness have been found to correlate with luminosity and mass of the galaxy and there is a continuous trend regardless of size. This means that dwarf galaxies are not a special type of galaxy, other than that they have low luminosity and mass. They are particularly interesting objects to study, since it is easier to get a broad overview of their chemical evolution than in a more complex galaxy. Because the galactic properties appear to follow a continuous relation, it is even more appropriate to deduce information about the chemical evolution on larger scales from these small systems.

To understand more about the chemical evolution of Boötes, Zn and Y will be measured in eight red giant branch (RGB) stars for this research. Fe, Mg and Ba will also be measured to compare the abundances found here, by using synthetic spectra, with the abundances found in an analysis of the same spectra, but with equivalent widths by Gilmore et al. (2013). By comparing abundances found in Boötes to those found in Sculptor and the Milky Way halo, it will be possible to find similarities and differences in chemical evolution for environments of different mass. Since the observed abundances are an indicator of the chemical abundances of the gas from which the star formed, the abundance measurements can also be used to study what type of supernova (SN) enriched this dwarf galaxy.

## 1.1 Different formation scenarios

Although it is becoming possible to study ever larger samples of resolved stars in the Milky Way from surveys like SDSS and in the near future Gaia, it is still difficult to unravel the chemical evolution of the Milky Way. There are multiple components, such as the halo and the bulge, each with their own properties. Dwarf galaxies can help, since they are smaller. By studying their chemical abundances and star formation histories, we can understand more about galaxy formation and evolution. There are different theories as to how galaxy formation has proceeded and studying dwarf galaxies may help to determine the exact formation scenario.

One of the possible paths for galaxy formation is monolithic collapse, as suggested by Eggen, Lynden-Bell & Sandage (1962). In this scenario, matter is able to cool and rapidly contract at early times. Because of conservation of angular momentum, a disk of gas will form and as this disk keeps cooling, it becomes unstable against gravitational collapse. Stars will form and a galaxy like the Milky Way is made.

The theory of monolithic collapse has been superseded by a scenario first proposed by Searle & Zinn

(1978) in which larger galaxies are formed from small, protogalactic clumps. This theory is called hierarchical merging and after the discovery of dark matter and dark energy, it developed into the  $\Lambda$ CDM model (e.g. White & Rees, 1978, Springel et al. 2005). It assumes that small dark matter halos formed first and the gas captured in these dark matter concentrations was able to cool and form stars. Because of gravity, these dark matter clumps move towards each other and continuously, they merge to form larger systems. It seems like a small step to next assume that dwarf galaxies are the building blocks of our galaxy and other large galaxies in the Universe. Carollo et al. (2007) concludes that the outer halo has formed from the merging of small systems within a pre-existing dark matter halo. Low-luminosity dwarf galaxies, such as Boötes, can be seen as the surviving systems for this scenario. Measurements of chemical elements play an important role in figuring out how the Milky Way has been assembled.

## 1.2 Chemical evolution

The paper *Synthesis of the Elements in Stars* by Burbidge et al. (1957) has been crucial in our understanding of how chemical elements in the Universe have formed. Several theories had been developed by that time, most assumed that all chemical elements were already formed in a very early phase of the Universe, just after the Big Bang. This would make for more or less static chemical abundances. The theory that was defended by Burbidge et al. was different since it “*proposed that the stars are the seat of origin of the elements*”. Different processes such as the *s*- and the *r*-process were proposed in the paper. The theory that nucleosynthesis in stars is responsible for most elements in the Universe is now firmly established. Chemical evolution has become an important area of study in astronomy. Measurements of chemical abundances from dwarf galaxies can be compared those to those measured in different populations of the Milky Way (e.g. Shetrone et al. 2001, Tolstoy et al. 2003, Venn et al. 2004). This comparison may be able to show if the Milky Way, or at least part of the Milky Way formed from these systems.

Fig. 1 shows that the chemical signature of most of the stars from dwarf spheroidals appears not to be that similar to any population of the Milky Way. This can be seen at  $[\text{Fe}/\text{H}] > -1.5$ , where  $[\text{Mg}, \text{Ca}/\text{Fe}]$  are clearly lower in the dSphs than in the Milky Way stars at the same metallicity, but even stars in dSphs with  $[\text{Fe}/\text{H}] < -1.5$  have  $[\text{Ca}/\text{Fe}]$  and  $[\text{Ti}/\text{Fe}]$  values lower than stars of similar metallicity in the Milky Way and the dSphs show a larger spread (Venn et al. 2004). This is only one of the differences between dSphs and stars in the Milky Way. These differences suggests that the merging scenario is not completely straight-forward. One of the conclusions is that while continuous merging is ruled out, early merging of low-mass dwarf galaxies is still possible, as well mergers from higher mass galaxies (Venn et al. 2004).

The decrease of  $\alpha$ -elements with increased  $[\text{Fe}/\text{H}]$  indicates the onset of SNe type Ia that chemically enrich their surroundings in Fe. The first stars to explode are the most massive ones, they will end in SN II explosions. Most  $\alpha$ -elements are produced in this type of SN. After some  $10^8 - 10^9$  years, less massive stars will also come to an end, some of them exploding as SNe Ia. This type of SN is the result of a white dwarf that has accreted mass from its binary companion. As a result of the increase in mass, the temperature in the white dwarf also increases and it will explode as a SN Ia. Both SN II and Ia produce Fe, but most Fe is produced by type Ia, while  $\alpha$ -elements come only from type II, resulting in a decrease in  $[\alpha/\text{Fe}]$  after the onset of SN Ia. This is seen as a turn-over in Fig. 1. For Sculptor, the knee is around  $[\text{Fe}/\text{H}] \sim -1.8$ . This should correspond to a timescale of about  $10^8$  to  $10^9$  years when SN Ia start contributing. Stars that fall before the knee in  $[\alpha/\text{Fe}]$  must have formed before this time. The place of the knee is dependent on star formation history and the efficiency and speed of chemical evolution and can therefore be at a different  $[\text{Fe}/\text{H}]$  in different galaxies.

## 1.3 The Boötes I dwarf galaxy

The large amount of uniform data from SDSS (York et al. 2000) has led to the discovery of numerous faint dwarf galaxies (e.g. Willman et al. 2005, Zucker et al. 2006a, 2006b and Belokurov et al. 2006, 2007). They typically have lower luminosities and are more metal-poor than the dSph galaxies that were

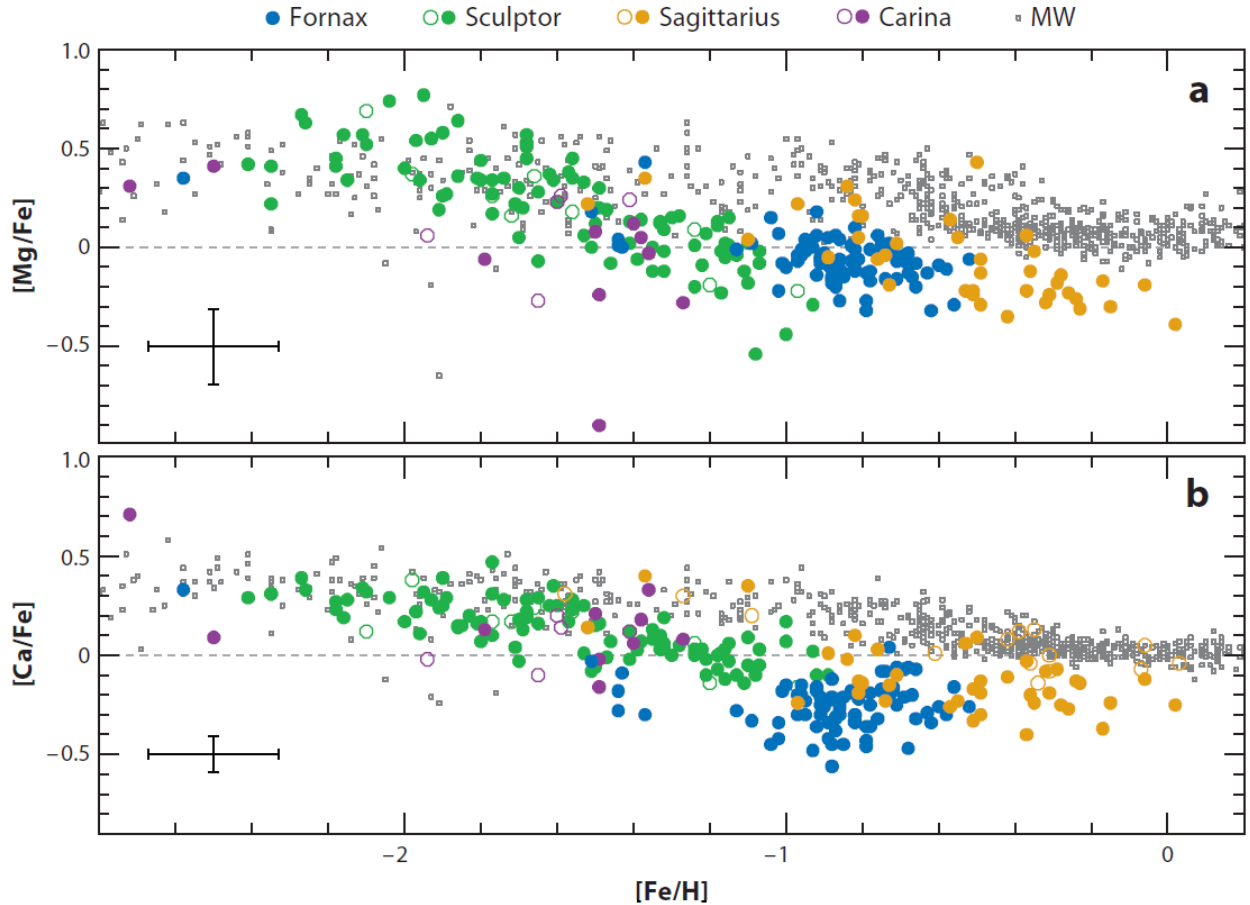


Figure 1: *Ca* and *Mg* abundances in four dSph galaxies and the Milky Way disk and halo. From Tolstoy et al. (2009) and references therein. Circles are dSphs, open circles are measurements from single-slit spectroscopy and filled ones are from multi-object spectroscopy. Grey squares are Milky Way disk and halo stars.

known before (Belokurov et al. 2007). One of those galaxies is Boötes I, first discovered by Belokurov et al. (2006). They found a luminosity of  $M_{tot,V} \sim -5.8$  mag. and a half-light radius of  $\sim 220$  pc. It does not have a well defined core and because of this, both Plummer and exponential profiles do not give a very good fit at the centre. From RR Lyrae variable stars, its heliocentric distance is determined to be 62 kpc (Siegel, 2006).

A large dark matter halo is assumed to surround dSphs to explain the high velocity dispersion of their stars and causing them to have a high mass-to-light ratio. This dark matter halo also separates them from globular clusters, which do not have a dark matter halo. For Boötes, the M/L was estimated by Koposov et al. (2011) to be 120, but other estimates go up to  $M/L \sim 1700$  (Wolf et al. 2010). The large difference in these estimates is mostly due to differences in the velocity dispersion. The data from Muñoz et al. (2006) that was used by Wolf et al. (2010) suggested an increase in velocity and velocity dispersion at a larger radius, while the analysis for the same stars by Koposov et al. (2011) does not show such a large increase. According to Koposov et al. (2011), the stars can be separated into a kinematic hot component with high radial velocity dispersion ( $9 \text{ km s}^{-1}$ ) and a cold component with low dispersion ( $2.4 \text{ km s}^{-1}$ ). They speculate that this could be the result of multiple star-forming regions merging around the time at which the dark matter halo of Boötes formed. A separation of stars into different kinematic components is seen in more dwarf galaxies, for example Canes Venatici I (Martin et al. 2007) and Sculptor (Tolstoy et al. 2004), both of which also show a difference in metallicity between two distinct kinematic components.

The stars that are studied in this research project all have  $[\text{Fe}/\text{H}] < -2.0$ , meaning that they are classified as very metal-poor stars (Beers & Christlieb, 2005). Some of them even fall into the extremely metal-poor category that contains stars with  $[\text{Fe}/\text{H}] < -3.0$ . Very metal-poor stars have only 1/100 the Fe abundance of that of the Sun, meaning that they formed from gas that was much less enriched by metals from earlier generations of stars than the gas from which the Sun formed. It may be possible that these very metal-poor stars have been enriched only by the first SNe, because Boötes has probably formed its stars in a short burst (Brown et al. 2014), so it did not have time for a more complicated chemical evolution.

## 1.4 Outline

The data used is described in Section 2 and a short summary of previous analysis of the data is also given here. The making of synthetic spectra is discussed in Section 3. This project was primarily observational, hence data reduction was a large part of the project and this will be discussed in Section 4. Results are in Section 5 and the analysis of these results is in Section 6. Section 7 discusses the types of zero-metallicity SNe that may have enriched Boötes. The discussion is in Section 8. At the end, the conclusions are presented in Section 9.

## 2 Spectroscopic data of Boötes

The UVES-fibre spectra used here have been analysed before by Gilmore et al. (2013, hereafter: G13) and the UVES-slit spectrum was analysed by Norris et al. (2010). Both analyses used equivalent widths to measure abundances, this analysis will use synthetic spectra to get more accurate abundances for weak lines or upper limits if the lines are too weak. Synthetic spectra are a more advanced and accurate method of determining the abundances than equivalent widths, which is why it is interesting to re-analyse the spectra again, using this method. The data used in this project are free to download from the ESO archive<sup>1</sup>.

### 2.1 The FLAMES-UVES spectrograph

The Very Large Telescope (VLT) that belongs to the European Southern Observatory (ESO) is located in the Atacama desert in Chile, on the mountain Cerro Paranal. It covers wavelengths in the infrared and the visible and consists of four telescopes with diameters of 8.2 metre, the first of which started operating in 1998. FLAMES, which stands for Fibre Large Array Multi Element Spectrograph (Pasquini et al. 2002), is one of the instruments on the Kueyen telescope<sup>2</sup>.

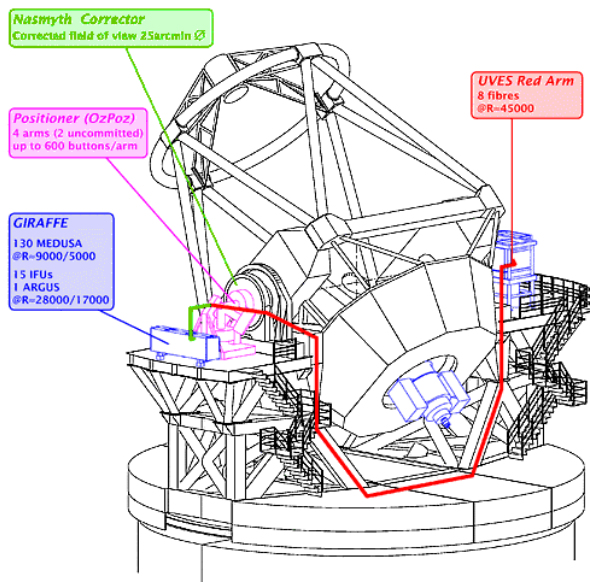


Figure 2: *FLAMES* spectrograph with the *OzPoz* plate connected to *GIRAFFE* and *UVES* [http://www.astropa.unipa.it/Telescopi\\_Ottici/VLT/FLAMES.gif](http://www.astropa.unipa.it/Telescopi_Ottici/VLT/FLAMES.gif)

FLAMES is a multi-fibre system that can feed to two spectrographs: GIRAFFE and UVES (Ultraviolet and Visual Echelle Spectrograph). This set-up is shown in Fig. 2. GIRAFFE has intermediate resolution,  $R \sim 5000 - 25,000$  and can observe spectra of more than 130 objects at a time. To do this, fibres are put on the relevant position and the light from that fibre is directed to the GIRAFFE spectrograph. UVES, which has a resolving power of  $\gtrsim 47,000$ , can be used in single-slit mode or up to eight fibres of 1 arcsec can be placed on the entrance aperture from FLAMES to fill the slit. One of the fibres should always be on the sky, for sky subtraction done in the data reduction. FLAMES has a fibre positioner (*OzPoz*) with two plates: one can be used to observe, while the other one is positioning fibres for the following observation. GIRAFFE and UVES-FLAMES can be used at the same time, but not for the same targets. When UVES is used in the fibre mode, three wavelength regions are available. They have central wavelengths of 520 nm, 580 nm, and 860 nm, cover a wavelength range of  $\sim 200$  nm and are all in the Red arm of UVES.

UVES is a cross-dispersed echelle slit spectrograph with two arms: one for UV to Blue and the other for Visual to Red (Dekker et al. 2000). It started regular observations in April 2000. In this setting, the resolution can be as high as 80,000 for the Blue arm and 110,000 for the Red arm when the slit width is adjusted.

<sup>1</sup><http://archive.eso.org/cms.html>

<sup>2</sup> The telescopes received names in the Mepuche language, which is spoken by a group of indigenous people living in Chile. Kueyen means “The Moon”.

## 2.2 Data

In G13, two groups worked independently on an analysis for 14 elemental species. The double-blind analysis was done to determine how accurate the abundances can be determined from spectra of similar quality to the ones used here. Both groups used equivalent widths to find abundances, but the linelists they used were not the same. After each group had measured the chemical abundances, a comparison was made. Differences were small and could mostly be assigned to differences in stellar parameters. For only a few stars, abundances for Zn and Y were determined.

For one Boötes star, Boo1137, a UVES-slit spectrum from a different set of observations was available. Norris et al. (2010) have analysed this star in detail, because of its low metallicity, which they found to be  $[\text{Fe}/\text{H}] = -3.7$ .

For this star, UVES Phase 3 data could be downloaded, this means that the spectrum is already reduced by the pipeline and sky-subtracted. The individual spectra only needed to be coadded and normalized. For the coadding, the same approach as described in the next section for the other stars was used, but only for the wavelength range 4600–5600 Å. Two other wavelength ranges were available, 3300–4500 and 5700–6600 Å, but they do not overlap with the range available for UVES-fibre, so they were omitted.

The total integration time for the seven UVES-fibre stars is 17.2 hr and for the UVES-slit star, it was 7.7 hr. Coordinates of the stars and photometric data in the *ugriz* photometry system are given in Table 1, data is from SDSS Data Release 12 (Alam et al. 2015<sup>3</sup>).

Table 1: *Coordinates and magnitudes of eight Boötes stars*

Star	R.A. (2000)	Dec.(2000)	<i>g</i>	<i>g</i> - <i>r</i>	Exposure time (hr)	UVES setting
Boo33	14 00 11.72	+14 25 01.39	18.23	0.76	17.2	fibre
Boo41	14 00 25.83	+14 26 07.58	18.38	0.72	17.2	fibre
Boo94	14 00 31.50	+14 34 03.56	17.50	0.89	17.2	fibre
Boo117	14 00 10.48	+14 31 45.50	18.20	0.76	17.2	fibre
Boo119	14 00 09.85	+14 28 22.97	18.43	0.74	17.2	fibre
Boo127	14 00 14.56	+14 35 52.73	18.16	0.79	17.2	fibre
Boo130	13 59 48.97	+14 30 06.20	18.20	0.71	17.2	fibre
Boo1137	13 58 33.81	+14 21 08.48	18.10	0.73	7.7	slit

## 2.3 Zinc, yttrium and zirconium

It is the aim of this work to measure abundances for Zn, Y and Zr in Boötes. These three elements are formed in different processes. For all three, the exact site where they are produced is not yet completely understood.

Zn is a volatile species, which means that it is almost undepleted onto dust grains, unlike most other elements. This is important for abundance measurements in damped Lyman-alpha systems (DLAs), which are used to study the neutral gas across a large range of redshift. Abundances of Zn in stars can be compared to those in DLAs, without having to estimate how much of the element is depleted. The environment in which Zn is produced is probably not the same as the place where Fe is produced however. While Fe is largely produced in SNe Ia, models predict that this is not true for Zn (e.g. Iwamoto et al. 1999). The production of Zn in massive stars depends on metallicity: more metal-rich stars produce more Zn (Fenner et al. 2004), leading to a time delay similar to that for Fe. It has been shown (e.g. Nissen & Schuster, 2011) that Zn abundances actually go down with  $[\text{Fe}/\text{H}]$  for stars in the Milky Way. Skúladóttir et al. (2016) showed that Zn in Sculptor also has  $\alpha$ -like behaviour. These results also suggest

<sup>3</sup><http://cas.sdss.org/dr12/en/tools/explore/summary.aspx>

that SN Ia do not produce large amounts of Zn.

Y is an element beyond the Fe-peak. Until Fe, nucleosynthesis in stars is producing energy by making heavier elements. The binding energy of elements reaches a maximum at Fe and making heavier elements requires energy. This means that the elements heavier than Fe must be formed by another process: neutron capture. There are two possibilities for this, slow neutron capture, or the *s*-process and rapid neutron capture, the *r*-process. For stars with  $[\text{Fe}/\text{H}]$  around solar, the *s*-process is the main source of Y, but for the metal-poor stars in this sample, Y is most likely produced by the *r*-process and an additional process that is sometimes called the LEPP or  $\nu\text{p}$ -process (Travaglio et al. 2004, Thielemann et al. 2011).

The origin of Zr is similar to that of Y, including the necessity of the  $\nu\text{p}$ -process. There may be a slight difference in nucleosynthetic origin of Zr and Y, because  $[\text{Y}/\text{Fe}]$  decreases a little for  $[\text{Fe}/\text{H}] \lesssim -0.6$ , while  $[\text{Zr}/\text{Fe}]$  seems to increase a bit, but this could as well be due to observational uncertainties (Travaglio et al. 2004). Abundances for Zr of halo stars (François et al. 2007) seem to follow the same pattern as those of Y, suggesting they indeed have a common origin.

In G13, using equivalent widths, Zn and Y could only be measured for a couple of stars and no conclusions could be drawn from this and for Boo1137, Norris et al. measured neither of these two elements. These elements are interesting to look at in the context of chemical evolution. The data will thus be analysed to find abundances of Zn, Y and Zr and three other chemical elements will be re-measured to compare the results from this analysis, using synthetic spectra, to the abundances derived by using equivalent widths.

### 3 Synthetic spectra

Analysing a stellar spectrum can be done by measuring equivalent widths or by using synthetic spectra. Measuring equivalent widths, as was done for example by G13 is the traditional approach. The equivalent width of a line is found by making a rectangle that has a height the same as the level of the continuum and with an area that equals that of the line. The width of that rectangle is the equivalent width. In some ways, it is more straightforward to go from equivalent widths to chemical abundances than to use synthetic spectra, because in the measuring of equivalent widths, no physics is involved. In going from equivalent width to abundance, an understanding of the physics involved is required, but for synthetic spectra, all lines have to be modelled and understood. A synthetic spectrum is a theoretical spectrum that a star with given stellar parameters, e.g. effective temperature and surface gravity, would have for certain chemical abundances. To make such a spectrum, stellar atmosphere models are needed as well as atomic libraries that describe the atomic transitions of lines at each wavelength. The stars used in this project are RGB stars, their cooler atmospheres result in spectra that are more complex, because there are numerous absorption lines, often from molecules. The lines in synthetic spectra are affected by the evolutionary phase of a star. Fig. 3 shows how stars with different spectral class and thus different surface temperatures have different spectra. The shape and lines are affected by the effective temperature. The largest difference between using synthetic spectra and using equivalent widths is that single, isolated lines are measured with equivalent widths, while for synthetic spectra the entire line profile is defined, including blended lines. Instead of treating the different elements separately, the synthetic spectrum shows how different abundances of one element can also change measurements of another element.

For this project, synthetic spectra were used because the lines from Zn and Y are very weak and at least upper limits to the abundances can be derived using synthetic spectra. If no line is visible, it is possible to change abundances in the model to see when the line would be visible, thus giving an accurate upper limit to the abundance of an undetected line. Another reason to choose synthetic spectra over equivalent widths, is that the lines in these spectra are more consistent with each other, as was explained before. There are two steps in generating synthetic spectra.

The first step in making a synthetic spectrum is to model the photosphere of the RGB star, since this is the layer from which radiation can escape. It is where the lines in a spectrum originate from. Several standard assumptions are often made in the modelling of stars, one of them is the assumption of Local Thermodynamic Equilibrium (LTE). This means that parameters like temperature vary very slowly and thus it is reasonable to say that a certain point is in thermal equilibrium with the neighbouring points. See Section 6 from Yong et al. (2013) for a discussion on expected non-LTE effects in stellar atmosphere models and synthetic spectra.

Another assumption that is usually made, is that the atmosphere of a star is plane parallel. This means that the stellar properties only vary with depth and the curvature of the star is not taken into account. It is assumed that we see the atmosphere as the same from all places. Limb darkening shows that this is not accurate. A more realistic approach is to use spherically symmetric models, especially for stars that have a thick photosphere compared to their radius, such as evolved giants. Both types of models are one-dimensional and this plays a role in the outer layers of late-type stars. The temperature structure in the models of these stars is determined by heating and radiative cooling, while in reality, expansion of the star also plays a role in cooling (Gustafsson et al. 2008).

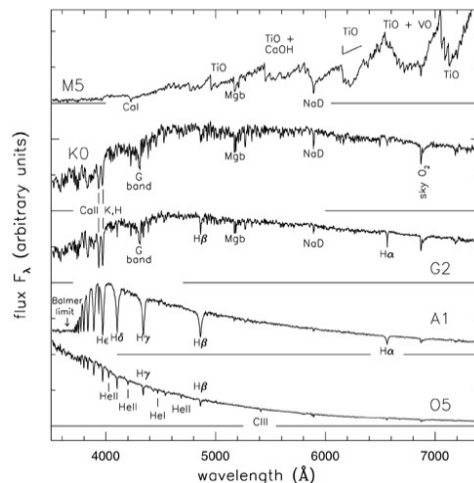


Figure 3: Spectra for stars with different spectral class (Sparke & Gallagher 2007)

### 3.1 MARCS models

MARCS models (Gustafsson et al. 2008) are stellar atmosphere models provided for a grid of stellar properties (e.g. surface gravity and effective temperature) of late-type stars. On their site<sup>4</sup>, there are about 52,000 stellar atmospheric models available for different spectral types. They have been developed and used since the 1970s (Gustafsson et al. 1975). One of the improvements made to the first models is that spherical symmetric models have been included alongside the original plane parallel models. LTE is still used, although others have developed model grids with non-LTE (Hauschildt et al. 2002). One of the reasons that Gustafsson et al. (2008) states for choosing LTE is that collision cross sections are not yet known accurately enough to use in the non-LTE models.

The necessary data files can be downloaded and a FORTRAN routine written by Thomas Masseron, which can then be used to interpolate between the models. Because some properties are not linearly varying between the grid points, interpolation is made a bit more complicated. This non-linearity has been taken into account in the code from T. Masseron. The routine, together with a user manual can also be found on the MARCS website.

Stellar atmospheres were calculated for each Boötes star individually by using the parameters found by NY and interpolating between the grid of MARCS models. Spherically symmetric models were used, because the stars are all red giants.

### 3.2 Turbospec

The output from MARCS that describes the stellar atmospheres can be used to calculate the stellar spectra using the Turbospec code which is described by Alvarez & Plez (1998) and can be downloaded from Plez (2012). For this research, version 15.1 was used. The code is also 1D and assumes LTE. Linelists for different elements should be provided and by setting parameters such as metallicity and turbulent velocity, a spectrum is created that spans the required wavelength range.

If only metallicity is specified, the other elements are assumed to have solar abundances. It is also possible to make spectra with different abundances. The linelists of chemical elements are from the Vienna Atomic Line Database (VALD, Piskunov et al. 1995). Synthetic spectra were made for the wavelength range 4600 – 5800 Å. The wavelength range can be specified. The observed spectra are in the range from 4600 to 5800 Å. An example of a synthetic spectrum together with the stellar spectrum being modelled is shown in Fig. 4. It covers the region of Mg I lines and some lines can be seen to give quite a good fit, but others do not fit particularly well. Since solar abundances are used, only [Fe/H] is set to  $-1.96$ , it is normal that not all the lines fit.

Turbospec gives a spectrum with a very high resolution and the width of the absorption lines is only determined by stellar parameters and abundances. This is how we would observe the spectrum if instruments were perfect. Since the resolution of UVES/FLAMES is not this high, the model spectra need to be convolved with a Gaussian to match the resolution of the UVES spectra. UVES has resolution 47,000 for our observations, but using this resolution on the synthetic spectra showed that the models still had a higher resolution than the stellar spectra. Smoothing with a resolution of 40,000 made the synthetic spectra look more like the observations. Fig. 5 shows how changing the resolution parameter in the Python module *instrBroadGaussFast* (from the package PyAstronomy.pyasl) influences the width of lines. A resolution of 30,000 is clearly too low and lines start blending, while the  $R = 47,000$  spectrum has lines that are a bit too narrow compared to the observed lines. Setting  $R = 40,000$  in *instrBroadGaussFast* corresponds to convolution with a Gaussian with a Full Width at Half Maximum (FWHM) of  $\sim 0.13$ .

Since the continuum of the stellar spectra was a bit higher than the continuum of the models, the models were also shifted upward by 0.01. This shift of about 1 percent is small and it corrects the difference between the stellar continuum and that of the models. These two changes to the models, the convolution and the small shift upward, will also be done for the models used in the abundance measurements, which will be discussed in Section 5.

---

<sup>4</sup><http://marcs.astro.uu.se/>

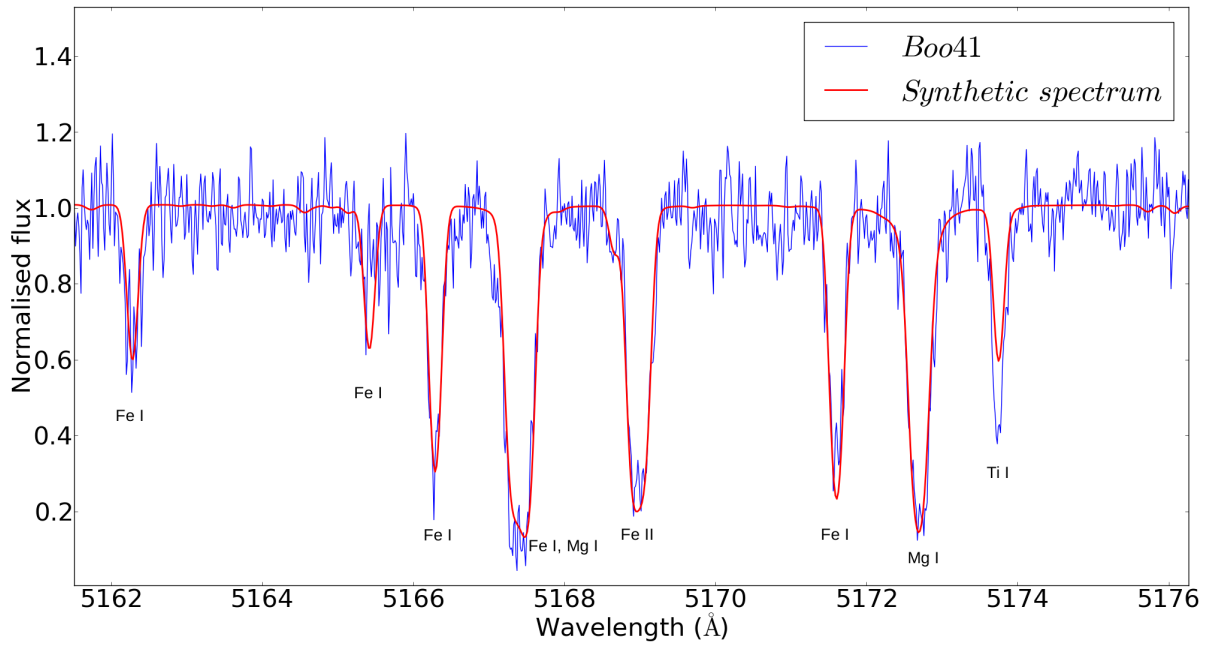


Figure 4: *Spectrum for Boo41 with its synthetic spectrum overlotted. All abundances are assumed to be solar in the synthetic spectrum, except  $[Fe/H] = -1.96$ .*

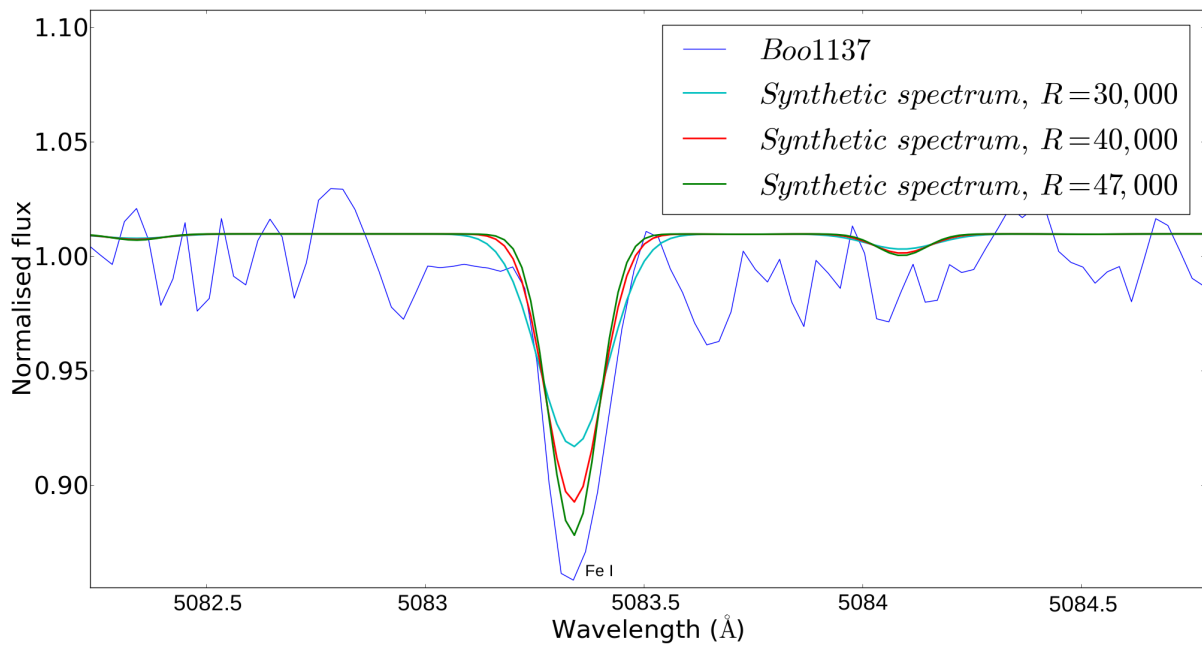


Figure 5: *Synthetic spectra convolved with Gaussians of different FWHM.  $R = 40,000$  shows the best resemblance to the spectrum of Boo1137.*

## 4 Data reduction

For much astronomical research, observations form the starting point. We have the advantage of modern instruments that can extract information from very faint objects. While the first astronomers could only use their eyes to learn about the stars and other celestial phenomena, we are aided by telescopes and instruments that keep getting better. Using instruments effectively also means taking into account that they are not perfect. Steps have to be taken to go from raw data to accurately calibrated data. Raw spectroscopic data, as used in this project, do not come with a wavelength scale and are dominated by sky background. Data reduction for the seven UVES-fibre stars involved several parts, some of them done automatically on ESO pipeline (Modigliani & Larsen, 2015). This step was not needed for the UVES-slit star. Information about the observation runs can be found in Table 2.

Table 2: *Record of observations for UVES-fibre and UVES-slit exposures*

UVES setting	Date of obs.	Exp. time (s)	Seeing	$v_{helio}(km\ s^{-1})$
fibre	17-02-2009	3300	0.72	22.25
fibre	18-02-2009	3300	0.78	22.06
fibre	18-02-2009	3500	0.69	21.95
fibre	19-02-2009	2750	0.68	21.76
fibre	19-02-2009	3350	0.82	21.67
fibre	24-02-2009	2750	0.69	20.28
fibre	24-02-2009	2750	0.66	20.19
fibre	24-02-2009	2750	0.69	20.08
fibre	24-02-2009	2750	0.73	19.98
fibre	01-03-2009	2750	0.64	18.34
fibre	01-03-2009	1600	0.8	18.23
fibre	02-03-2009	2750	0.6	18.02
fibre	02-03-2009	2750	0.99	17.9
fibre	05-03-2009	3050	0.96	16.78
fibre	18-03-2009	2750	0.86	11.99
fibre	18-03-2009	2750	0.75	11.66
fibre	18-03-2009	2750	0.81	11.54
fibre	18-03-2009	2750	0.84	11.43
fibre	20-03-2009	2750	0.6	10.9
fibre	20-03-2009	2750	0.7	10.78
fibre	21-03-2009	2750	0.64	10.39
fibre	30-03-2009	2750	0.84	6.05
slit	24-04-2009	2753	0.73	-4.84
slit	24-04-2009	2753	0.96	-4.94
slit	24-04-2009	2753	0.8	-5.04
slit	24-04-2009	2753	0.76	-5.14
slit	24-04-2009	2753	0.62	-5.23
slit	25-04-2009	2753	1.03	-5.27
slit	25-04-2009	2753	0.67	-5.37
slit	25-04-2009	2753	0.63	-5.47
slit	25-04-2009	2753	0.71	-5.57
slit	25-04-2009	2753	0.89	-5.66

### 4.1 The FLAMES-UVES pipeline

There is a publicly available ESO pipeline for FLAMES-UVES (Modigliani & Larsen, 2015). Spectra for the stars from Boötes and calibration files such as flatfields are also available and are needed for the pipeline reduction. A detailed description of all the steps and parameters in the pipeline can be found in the user manual (Modigliani & Larsen, 2015). A summary will be given here and additional information about the settings will be mentioned when needed.

The *Reflex* workflow was used to organise the data for further processing with the pipeline. All the data reduction steps are shown in a window as in Fig. 6 and parameters can be set as required. The settings for optimum extraction (OPT) were used, this is the default setting for the pipeline. It provides an optimal signal-to-noise ratio, unlike the average (AVG) settings, which simply averages any signal that is above the sky background level.

As a first step, the *Reflex* Data Organiser makes groups of the available datasets. It determines which calibration files belong to which science frames and what each calibration file is, e.g. dark frames, flat fields or bias frames. It is then possible to select the datasets that should be reduced by the pipeline. The advantage of using *Reflex* instead of another tool such as EsoRex, is that the data organisation is done by the workflow. All that needs to be provided are the calibration and science frames.

Even if there is no light detected by the telescope, the CCD still registers a signal, this is the bias. It is present in all exposures and needs to be subtracted. This is done by taking bias frames, which are readouts of the CCD without integration time and with the shutter closed. By taking the median of these bias frames, a Master Bias is created which can then be subtracted from all the other frames.

The bias is not the only thing that contributes to a signal in the CCD, even when there is no light detected. There is always some noise present from the different pixels in the CCD. This can come from hot pixels or noise from the CCD that is not random. Since exposure time influences this, dark frames of similar integration time as the science frames should be made. These are combined to make a Master Dark to look at these properties of the CCD and, if possible, to correct for them.

Flatfielding is the next step. There are two types of flatfields that are used by the pipeline. First, there are the slit flat-fields that are taken with the shutter open and a light source, to highlight the imperfections in the illumination of the CCD. An example of this is when the sides of an image receive less light than the centre. Differences in efficiency of the detector over the field of view need to be taken out. There can always be outliers due to cosmic rays for example, so again, a Master Slit Flat-field is created from combining multiple flat-fields with a sigma clipping algorithm. Instead of subtracting this from the science frames, the science frames should be divided by the Master Flat to correct them.

Next, spectra from a ThAr arc lamp are needed to determine the wavelength scale of the spectra. The wavelengths of the lines from the ThAr lamp are known and stored in a reference table. This information can be used to determine the orders and the wavelength calibration. Both are needed for the wavelength solution.

Other calibration files include single fibre order definition frames. A continuum lamp is used to illuminate only one fibre and the resulting image shows the locations of the fibre orders. It needs to have a very high signal-to-noise to be able to clearly distinguish all the orders.

To obtain the final spectra, fibre flatfields are needed to correct for differences in fibre throughput and fibre positions in the UVES slit. Because the fibres are very close to each other, there will be overlap between the profiles from neighbouring fibres. To correct for this in the pipeline, there are flatfields with only the odd numbered fibres and ones with only even numbered fibres. In these odd-even frames, signals from different fibres can be distinguished. To correct for differences in fibre throughput, a flatfield of all the fibres at the same time is also taken.

The last step is to obtain a final, accurate wavelength solution. Previously, only one fibre was illuminated by the ThAr lamp, but to get a more accurate determination of the solution, this should be done for all fibres. A wavelength solution can now be made for all science frames. This will give final science spectra that are wavelength calibrated.

Since it was not completely clear from the documentation whether the pipeline had also done sky subtraction or not, this needed to be checked. It was obvious that no sky subtraction had taken place, since there was a clear sky line visible at 5577 Å. This line was useful to determine if the pipeline did correct for fibre throughput. Each fibre has a different throughput and this should be corrected. For

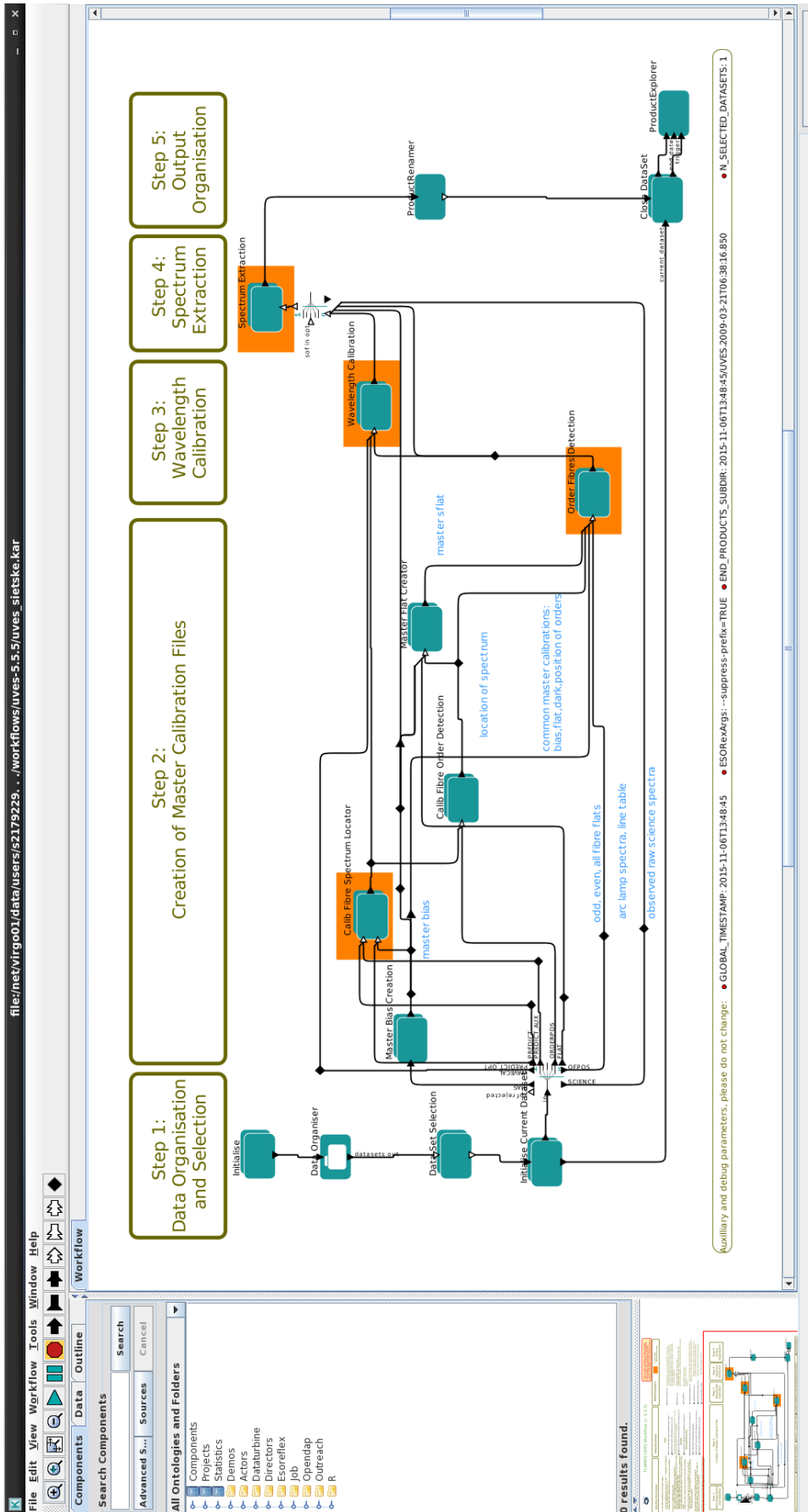


Figure 6: The Reflex workflow shows the steps done in the pipeline processing of the raw data.

all datasets each fibre was assigned to the same star, so it was possible to just look if the sky line was systematically stronger or weaker in different stars. The height of the sky line in the spectra for the stars was divided by the the height of the line in the sky spectrum. When the average (for each star) of the 22 data frames was taken, the maximum difference was 0.12. For the brightest star (Boo 94), the height of the line was largest and the weakest star (Boo 119) had the lowest height. The stellar continuum is higher for the brightest star and lowest for the faintest, so this difference in the height of the sky line is due to a difference in brightness of the stars.

## 4.2 Sky subtraction

After running the pipeline and checking the results, sky subtraction could be carried out. There are several ways to do this and it can depend on the data which one works best. Finding out what worked took some time, as the spectra kept showing “wiggles”. Fig. 7 shows an exaple of this problem. Trying to get rid of them involved a lot of experimenting with sky subtraction. Some of the options that were tried will be summarised here.

Each individual observation consisted of seven stellar spectra and one sky spectrum, all taken at the same time. The most simple way to do sky subtraction would be to just subtract the sky spectrum belonging to that observation from all the spectra. However, this is not the best way to do sky subtraction, since a sky spectrum shows a lot of noise. By just subtracting, you are basically adding noise to the already faint target stars. The main reason for trying this was to see if the wiggles would disappear. They did not.

Another method that is not much more difficult is to smooth the sky by a certain number of pixels to decrease the noise in the spectrum and subtract this smoothed spectrum. The sky spectrum could be smoothed by 401 pixels in IRAF before the shape of the spectrum was lost. This was done for the complete spectrum, except for the strong sky line. Smoothing a sky line would result in a much weaker, but broader line. This would mean that a much larger part of the final spectrum would be affected by the sky line, while it is only present in a small region. The smoothed sky with sharp sky line is subtracted from the stellar spectra.

Since there are multiple observations, it was also possible to average the sky spectra to a single sky and, being either smoothed or not, this single spectrum can be subtracted.

We found that subtracting the sky spectrum taken for the same set as the observations, but smoothed by 401 pixels gave the best results. The wiggly shape of the spectrum proved to be normal for stars that have such a low flux. It is probably a result of the different orders from the spectrograph that are imperfectly combined in the pipeline. As a side note: changing the parameters *merge\_delt1* or *merge\_delt2*, that influence the amount of overlap of different orders and can be found in *flames\_obs\_scired*, did not help either.

We are now at the point where all individual spectra are all wavelength calibrated and sky subtracted, but they are not yet combined.

## 4.3 Coadding and normalizing spectra

Because the observations for the stars were spread out over several nights spanning more than a month, the frames need to be corrected for the heliocentric velocity. Heliocentric velocities can be calculated with IRAF task *rvcorrect*. Another IRAF task, *dopcor*, could then be used to shift the spectra by the desired amount.

For each star, all heliocentric velocity corrected exposures can be combined to provide a coadded spectrum. Conditions such as seeing may change between different exposures resulting in different signal-to-noise (S/N) for each exposure. This means that a simple average of the different exposures is not the

best approach, but a weighted average takes the varying data quality better into account. Weights were based on S/N, such that exposures with higher S/N would get a greater weight. To get rid of cosmic rays, sigma clipping ( $3\sigma$ ) around the median was used. The sigma clipping should be done around the median, not around the average, since large outliers can have a significant effect on the average and the goal of sigma clipping is to remove these outliers. IRAF proved helpful again in coadding the spectra: the task *scombine* can make a weighted average, with sigma clipping.

Sigma clipping for  $2\sigma$  was also tested, but this gave a slightly lower S/N than the  $3\sigma$  clipping. Only Boo94, the brightest star, had a higher S/N for  $2\sigma$  clipping, but because all the other gave better results with  $3\sigma$ , the latter was used for all stars.

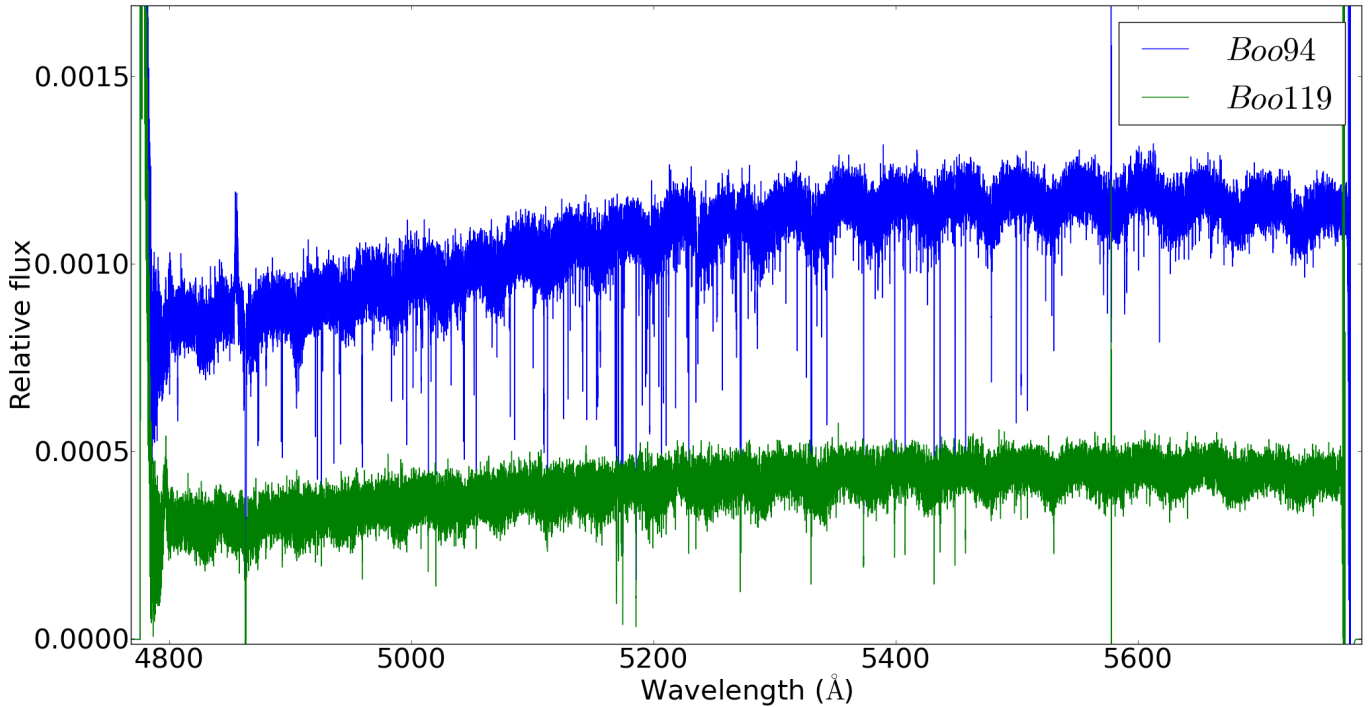


Figure 7: Coadded spectra of *Boo94* and *Boo119*, not normalized. Both spectra show wiggles due to overlap between different orders.

The coadded, but not yet normalized, spectra of two of the Boötes stars can be seen in Fig. 7. Boo94 can clearly be seen to increase in flux towards the red end of the spectrum. This is because the red giant simply emits more at redder wavelengths, but also because the sensitivity of the CCD is better at these wavelengths. The final spectrum should not show this shape. In regions where there are no lines, but just continuum, the spectrum should be flat and it can be normalised. This normalisation is the last step to have a spectrum that is ready for analysis. To find the continuum regions of the spectra, synthetic spectra were made as described in Section 3.

By fitting a polynomial of the third order to linefree regions found with the synthetic spectra and dividing the stellar spectrum by this polynomial, the normalized spectrum is obtained. Fitting a polynomial of higher order did not change the normalised spectrum significantly, so a second order fit was chosen. The initial stellar parameters for effective temperature ( $T_{eff}$ ), surface gravity ( $\log(g)$ ), metallicity ( $[\text{Fe}/\text{H}]$ ) and microturbulent velocity ( $\xi_t$ ) of each star are from the Norris and Yong (hereafter: NY) analysis in G13. Their stellar parameters can be found in Table 3, together with the parameters for Boo1137 from Norris et al. (2010). As the next step, the stellar absorption lines in each stellar spectrum will be used to find the abundances of chemical elements.

Table 3: *Stellar parameters from G13*

<b>Star</b>	<b>S/N (at 5300 Å)</b>	<b><math>[\text{Fe}/\text{H}]_{NY}</math></b>	<b><math>T_{eff,NY}</math> (K)</b>	<b><math>\log(g)_{NY}</math></b>	<b><math>\xi_{NY}</math></b>
Boo33	19	-2.36	4730	1.4	2.8
Boo41	18	-1.96	4750	1.6	2.8
Boo94	32	-2.97	4570	0.8	3.3
Boo117	18	-2.31	4700	1.4	2.7
Boo119	16	-3.21	4790	1.4	2.4
Boo127	21	-2.11	4670	1.4	2.7
Boo130	16	-2.35	4750	1.4	2.6
Boo1137*	51	-3.7	4700	1.2	2.2

\* From Norris et al. (2010)

## 5 Results

Once the spectra of all the stars in the sample are wavelength calibrated, sky subtracted, coadded and normalized and the synthetic spectra are set up, then the analysis can be done. The goal of this project is to get abundances for Zn and Y, which were only measured sporadically by G13. Other elemental abundances (Fe, Mg, Zr and Ba) have also been measured to compare with those in G13 and to make sure their stellar parameters are consistent with our synthetic spectra. Abundances for element X from the synthetic models are given in absolute abundances,  $\log \epsilon(X)$ :

$$\log \epsilon(X) = \log_{10}(N_X/N_H)_* + 12$$

Here,  $N_X$  is the number of atoms of chemical element X per unit volume and  $N_H$  is thus the number of hydrogen atoms per unit volume. From this, the abundance of element X relative to another elements can be calculated:

$$[X/Y] = \log_{10}(N_X/N_Y)_* - \log_{10}(N_X/N_Y)_\odot$$

Solar abundances are needed to calculate this relative abundance. Solar abundances of Asplund et al. (2009) were assumed here. When needed, data from other work is scaled to be consistent with these solar abundances.

### 5.1 Iron

Iron is the element with most lines and it is a fundamental component in stellar atmosphere models. It is the starting point for all abundance analyses and the ratio of other elements to Fe is often used when analysing the stellar abundances. It was of course measured in G13, so it is possible to make a comparison with their values. Thus, it was also used as a check that the data reduction and analysis presented here went well and as a proof that their stellar parameters ( $T_{eff}$ ,  $\log(g)$ ,  $\xi_t$ ) could be used to make the model spectra.

The Fe I lines from the NY analysis (G13) that are in the wavelength range considered here are used to measure  $[\text{Fe}/\text{H}]$ . Since only the lower wavelength range of UVES is used, this means all lines of Fe I, up to the one at 5615.64 Å, which are 56 unblended lines in total. The linelist used is given in Appendix A. Turbospec was used to make synthetic spectra with different Fe abundances. A Python program that calculated the chi-square for each line was used. The model with the minimum chi square value corresponds to the best fitting Fe abundance. A comparison of the values for  $[\text{Fe}/\text{H}]$  with those from NY showed that the synthetic spectra lead to lower  $[\text{Fe}/\text{H}]$ . For Boo94, the average offset is  $-0.22$  dex. Shifting my abundances up by this amount showed that the residual difference between both measurement was mostly within the errors of NY, see Fig. 8. There is more scatter for lower  $[\text{Fe}/\text{H}]$ , meaning that the weak lines can be difficult to measure correctly. The difference from the other analysis in G13, done by Geisler and Monaco (GM), with that of NY is also shown in Fig. 8. Their scatter is also larger for lower  $[\text{Fe}/\text{H}]$  and is similar to the scatter from the analysis with synthetic spectra. There is no trend of the scatter with wavelength, which is shown in Fig. 9 for the equivalent widths but is also true for  $[\text{Fe}/\text{H}]$ .

Since the abundances should in principle agree for both analyses, the analysis and data reduction were carefully checked to make sure that the difference is due to the different way of measuring abundances. Part of this check was to measure the equivalent widths for the Fe lines. This is shown in Fig. 9, where the difference in equivalent width is plotted against wavelength and the strength of the line is shown by a colourbar. Blue lines are the weakest and red lines are strongest. Scatter is independent of the strength of the line. The average offset of equivalent widths determined here from those measured by NY is  $\sim -0.88$  Å and the standard deviation is 3.3, this is shown in Fig. 9. This difference is too small to cause the observed difference in  $[\text{Fe}/\text{H}]$ .

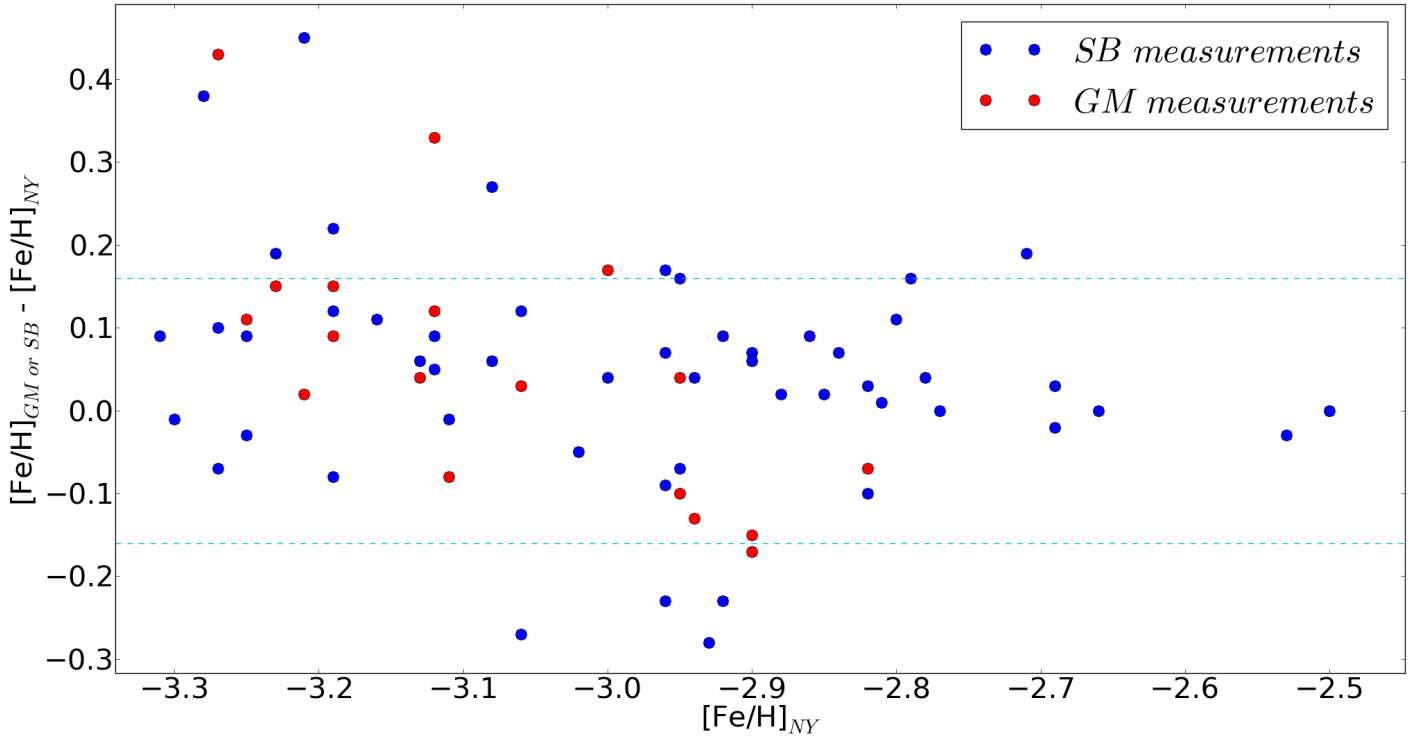


Figure 8: Difference between  $[Fe/H]$  measured here and that of NY from G13 for 52 individual lines of Fe for Boo94. This difference is shifted by  $+0.22$ . The difference between the two analyses in the paper, GM and NY is also shown for 18 Fe lines. Note that GM used a different linelist from NY. Dashed cyan lines show the error on  $[Fe/H]$  in NY.

The conclusion from Figs. 8 and 9 is that a simple shift can account for the difference for  $[Fe/H]$  between both measurements and there is no trend of scatter with wavelength. Since equivalent widths of the re-analysed spectra are similar to those from NY, the difference in  $[Fe/H]$  is not from an error in the re-analysis but due to a difference between making an analysis with synthetic spectra and using equivalent widths. Both figures are for one star, Boo94, but they look similar for other stars, with some differences in offset.

Fig. 10 shows the difference between  $[Fe/H]$  determined here with that from NY against wavelength. Equivalent widths of the lines from NY are colour coded: strong lines with high equivalent widths are red, weaker ones are green and the weakest lines are blue. The lines for which spectral synthesis finds a too high  $[Fe/H]$  w.r.t. measurements from NY are weak lines, with small equivalent width. Because they are difficult to measure accurately, it is expected that they have more scatter. Most measurements fall within the errors of NY when a shift of  $+0.22$  is applied, but there are four lines that fall below the error. These lines are between  $5300 - 5500 \text{ \AA}$  and are lines with large equivalent widths. A low  $[Fe/H]$  from synthesis could mean that there is a problem with the wings of strong lines. However, changing the region over which the chi square matching between model and data is calculated to make sure that these wings are included does not give a different result. It can be difficult to get reliable abundances for strong lines, since they can have wings that extend over a larger wavelength range than the range that is taken into account. Because of this, lines with equivalent width  $> 150 \text{ \AA}$  were left out in the determination of  $[Fe/H]$ . Similar to sigma clipping that was used in the coadding of spectra, all lines that differed by more than  $2\sigma$  from the average difference between the synthetic  $[Fe/H]$  and  $[Fe/H]_{NY}$  were also left out.

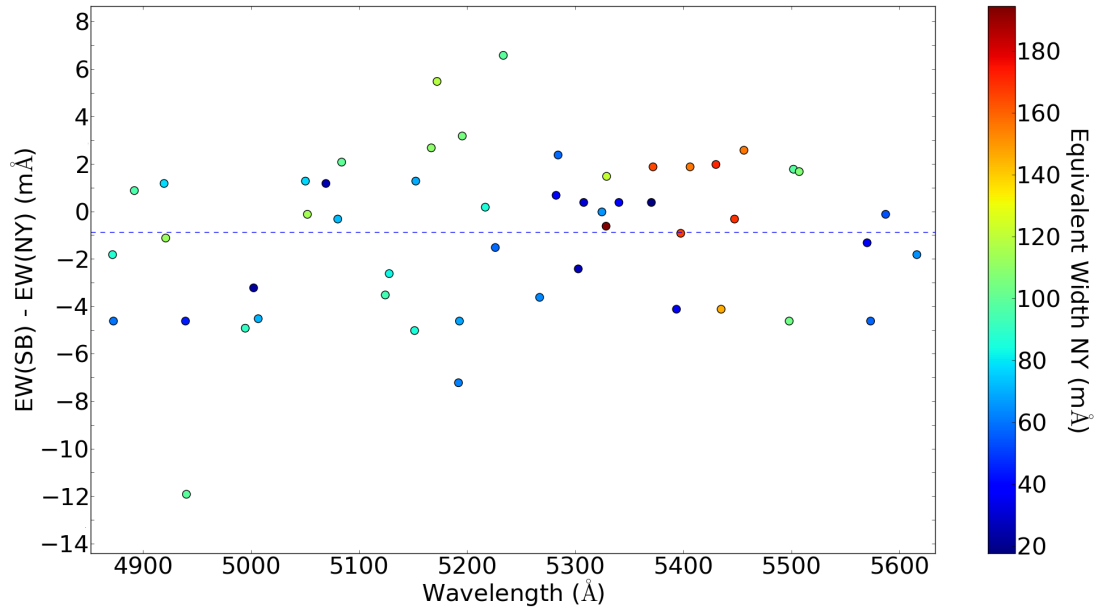


Figure 9: Difference between equivalent widths measured here and those of NY for 52 individual lines of Fe for Boo94. The blue dashed line is the average difference ( $\sim -0.88$ ) between them.

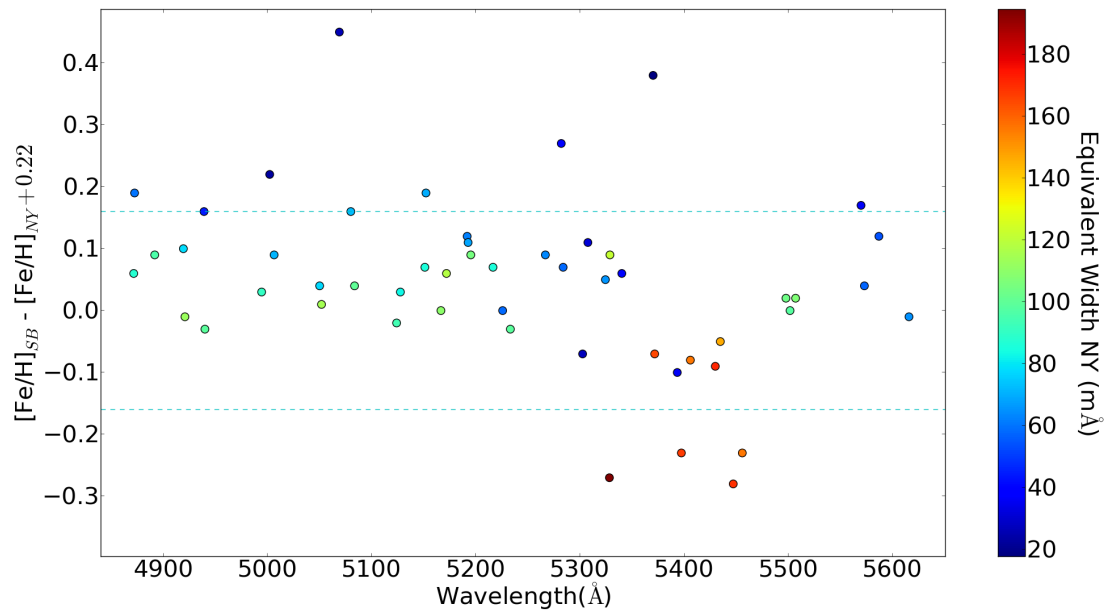


Figure 10: Difference of synthetic  $[Fe/H]$  with that of NY together with equivalent width of NY. Data points are shifted by  $+0.22$  to correct for the average offset. Dashed cyan lines give the error on  $[Fe/H]$  in NY.

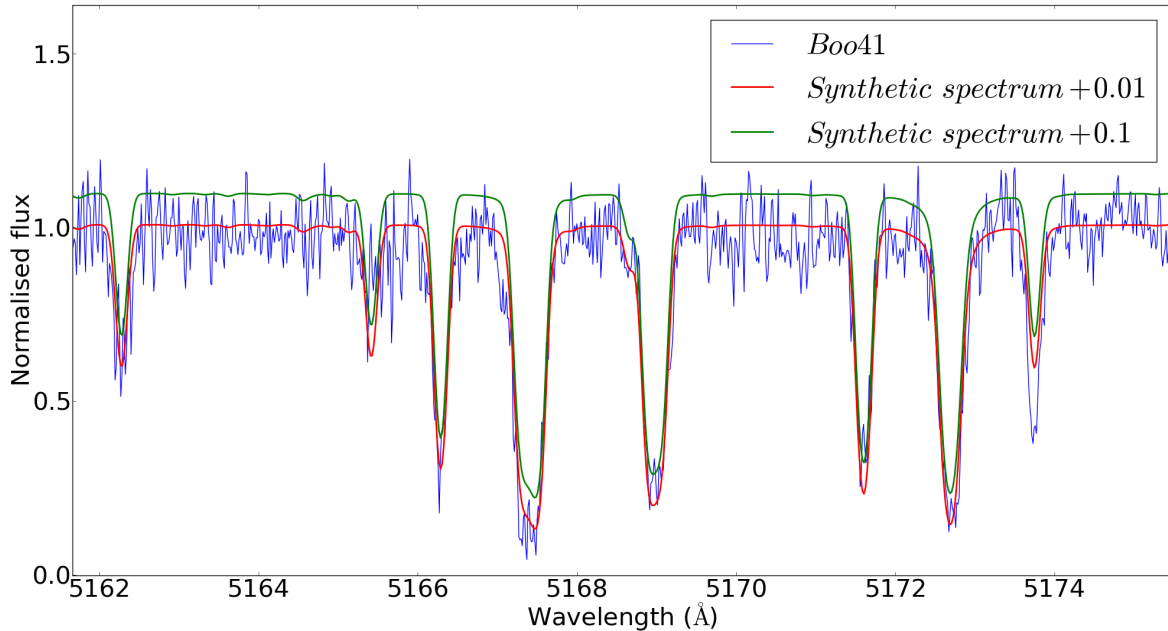


Figure 11: *Spectrum of Boo41 with two synthetic spectra: red is +0.01, green is +0.1. The wavelength region shown is the same as in Fig. 4.*

To reduce the offset with NY, it is also possible to change the continuum of the synthetic spectra slightly upwards. The shift should be about 0.1 dex, which is too high to be realistic. Since it is possible that the continuum was a bit off, this was the point where the shift of 0.01 dex for the models was introduced. Fig. 11 shows that the synthetic spectrum shifted upward by +0.1 is too high compared to the stellar spectrum of Boo41. The synthetic spectrum that is shifted by +0.01 agrees well with the stellar spectrum. This resulted in the final difference with NY to be  $-0.1$  dex, when averaged over all the stars. Values for  $[Fe/H]$  and the difference between both measurements are listed in Table 4.

Table 4: *Difference between  $[Fe/H]$  determined with synthetic spectra (SB) and that determined by NY*

Star	SB $[Fe/H]$	NY $[Fe/H]$	Difference
Boo33	-2.41	-2.37	-0.04
Boo41	-2.17	-1.96	-0.21
Boo94	-3.06	-2.98	-0.08
Boo117	-2.41	-2.32	-0.09
Boo119	-3.30	-3.21	-0.09
Boo127	-2.22	-2.13	-0.09
Boo130	-2.50	-2.37	-0.13
Boo1137	-3.72	-3.66	-0.06
Average	-2.72	-2.63	-0.10

When measuring equivalent widths, the wiggles in the spectrum are not that much of a problem, since the continuum around the lines can be defined by hand. With synthetic spectra however, this is not possible and the wiggles may affect the best fit abundances. At the top of a wiggle, the stellar spectra have a higher continuum than the model. Lines from the star are thus also shifted, which would result in lower abundance measurements from the synthetic spectra. The opposite would happen at the bottom of a wiggle: lines start at a lower point and the corresponding line in the synthetic spectrum should be deeper, resulting in an abundance measurement that is higher than in reality. To see if this trend of follows the pattern of wiggles, a comparison was made of the difference in abundance for each line with

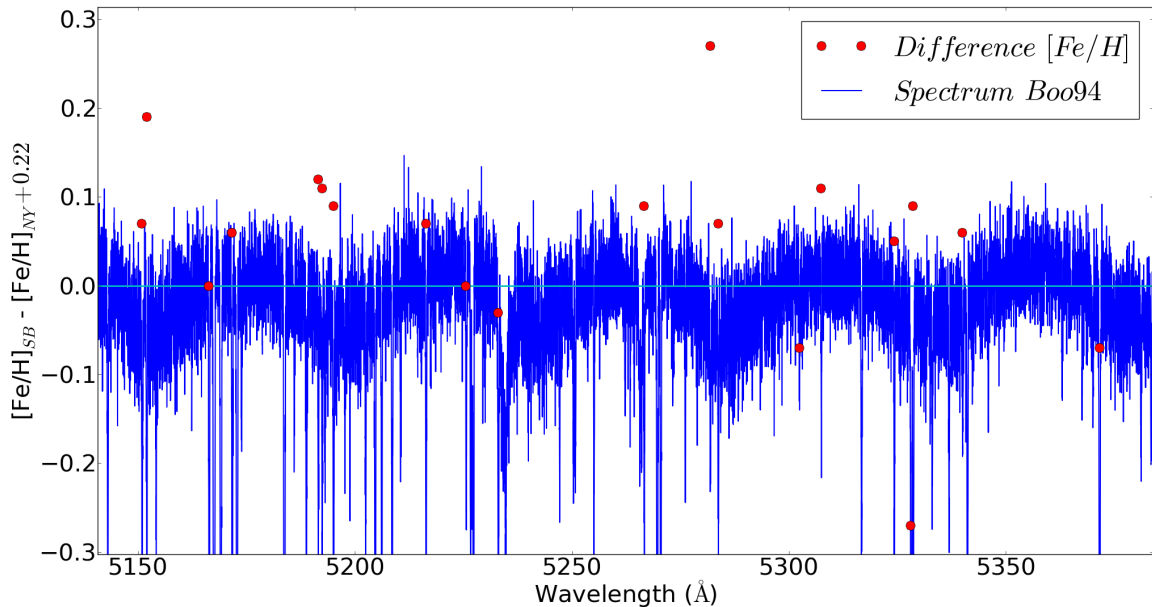


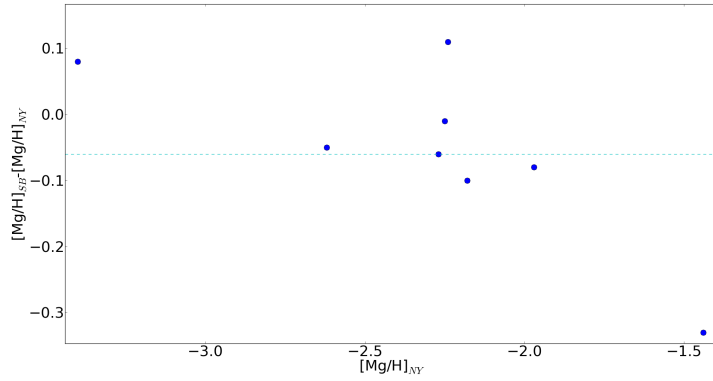
Figure 12: *Difference of synthetic  $[Fe/H]$  with that of NY, shifted by  $+0.22$  (red points), together with the normalised stellar spectrum of Boo94, shifted by  $-1.0$  (blue line). The cyan line is where  $[Fe/H]_{SB} - [Fe/H]_{NY} + 0.22 = 0$ .*

those of NY against wavelengths at which the stellar spectrum had a peak or a valley. For some points, a correlation seemed to exist, but no clear pattern could be discerned, this is shown in Fig. 12. At some places, the Fe line is at the minimum in the stellar spectrum, but  $[Fe/H]_{SB} - [Fe/H]_{NY} + 0.22 > 0$ , meaning that the synthetic spectra measure a higher  $[Fe/H]$  than NY (after correcting for the average offset). This is expected if the difference between the two analysis is due to the wiggles. At other places, however, the peaks in the stellar spectrum correspond to  $[Fe/H]_{SB} - [Fe/H]_{NY} + 0.22 > 0$ , while a difference  $< 0$  would be expected if there were a pattern. Thus, the apparent correlation could be produced by chance.

Finding no clear correlation with abundance scatter and the wiggles in the spectrum does not directly mean that the wiggles should be ignored. One possibility to correct for them is to take the local continuum around the wiggles and then calculate the best fit abundance of the lines in that part. This is consistent with treating each order separately to correct for the wiggles. After this, the abundances changed by less than 2 percent. Since there are a lot of Fe I lines and they are all strong enough to be measured (a very weak line could disappear if it would be placed at the top of a wiggle), I chose to not correct for the wiggles in the case of  $[Fe/H]$ . A correction would only change abundances by a small amount, if they would change at all. For other elements that do not have this many lines and if the lines are very weak, the continuum was defined locally. Measurements of other elements will be discussed in the next subsections and for these elements, the spectra are locally normalised.

## 5.2 Magnesium

To make a comparison between the NY analysis and that from synthetic spectra, Mg was also measured. Mg is one of the  $\alpha$ -elements, thus it is typically enhanced in the old stars of Boötes. Three unblended lines were used to determine  $\log \epsilon(\text{Mg})$  and this was then compared to the abundances derived by NY. In some cases, e.g. Boo117, there is a large difference between both methods, but the errors are of the order 0.2 for both, so the measurements are consistent within the errors.



In Fig. 13 it can be seen that the difference between the abundances  $\log \epsilon(\text{Mg})$  are  $\lesssim 0.1$  dex.

Figure 13: *Difference between  $[\text{Mg}/\text{H}]$  from synthetic spectra and that determined by NY with equivalent widths. The average difference is  $-0.06$  dex and is shown by the dashed cyan line. The largest difference is for Boo117, at  $[\text{Mg}/\text{H}]_{\text{NY}} = -1.44$ .*

Fig. 14 shows  $[\text{Mg}/\text{Fe}]$  for stars in Boötes and for stars in the Milky Way halo.

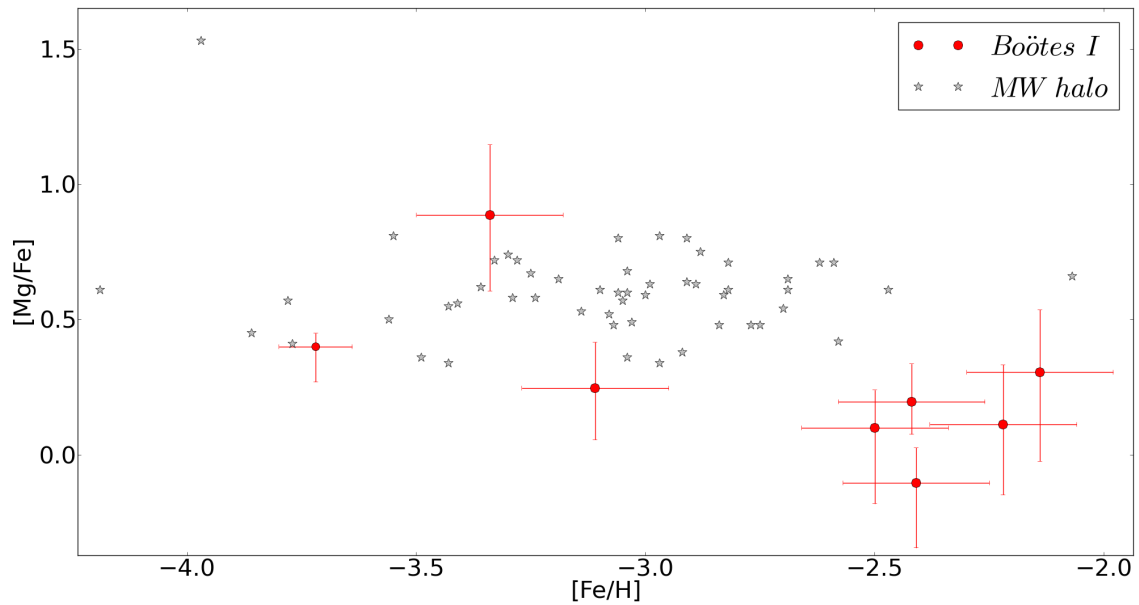


Figure 14:  *$[\text{Mg}/\text{H}]$  for RGB stars in Boötes (red dots) and in the Milky Way halo (grey stars, Cayrel et al. 2004, Andrievsky et al. 2010).*

### 5.3 Barium

Ba has strong lines and could be measured in all of the stars. It was also measured by NY and a comparison of both measurements is made in Fig. 15. There is a systematic offset for the abundances determined by using the synthetic spectra:  $[Ba/H]_{SB} - [Ba/H]_{NY} \approx -0.19$  dex on average. This is probably again caused by using synthetic spectra instead of equivalent widths to analyse abundances. The comparison is made by only using one line, at 4934.08 Å. For most stars, NY used two or three more lines, but they were not in the wavelength region used in this project. Ba abundances determined by the synthetic spectra will be used for the remaining analysis.

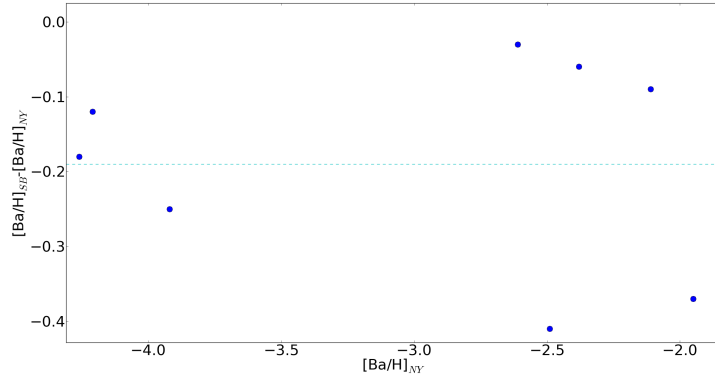


Figure 15: *Difference between  $[Ba/H]$  from synthetic spectra and that determined by NY with equivalent widths. The average difference is  $-0.19$  dex and is shown by the dashed cyan line.*

A comparison of  $[Ba/Fe]$  in Boötes and in the Milky Way halo is shown in Fig. 16.

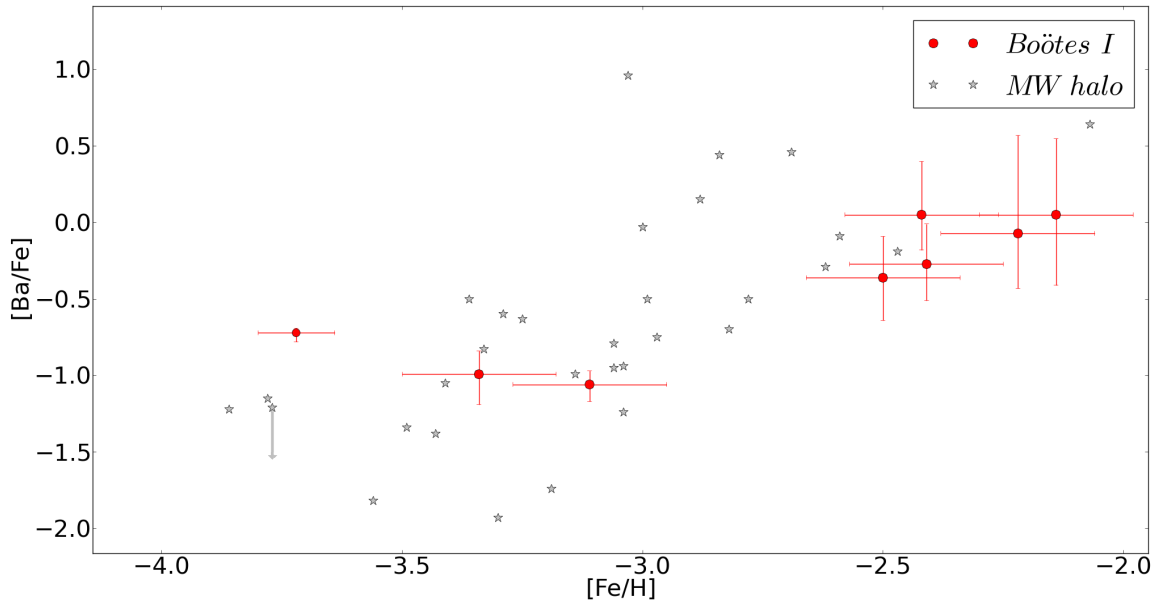


Figure 16:  *$[Ba/Fe]$  for stars in Boötes and the Milky Way halo (Cayrel et al. 2004, François et al. 2007). Symbols as in Fig. 14.*

## 5.4 Zinc

Zn is one of the key elements of this research. One line, at  $4810.5 \text{ \AA}$  could be seen in most spectra. The line is very weak and therefore difficult to measure, but with synthetic models, it was possible to get abundances for five out of eight stars and for the other three, accurate upper limits could be derived. The abundances for the stars of Boötes and the Milky Way halo can be found in Fig. 17.

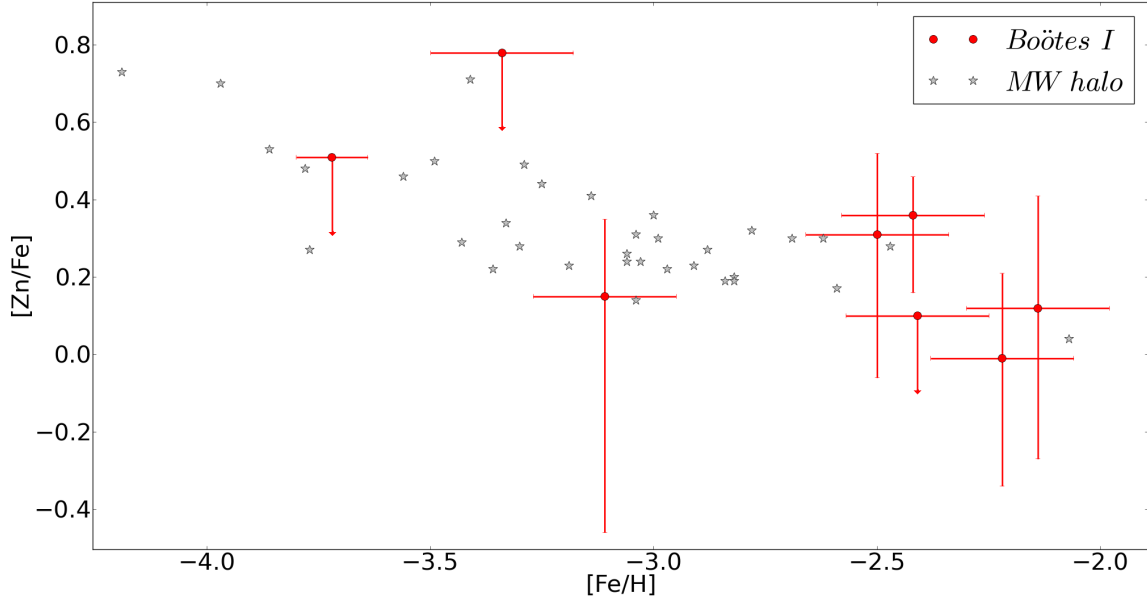


Figure 17:  $[Zn/Fe]$  for stars in Boötes and the Milky Way halo (Cayrel et al. 2004). Symbols as in Fig. 14.

## 5.5 Strontium

For Sr, the lines were too weak to be measured, there was just noise in all the spectra. The lines at  $4811.88$  and  $4962.26 \text{ \AA}$  were also slightly blended, making them not ideal to determine abundances and they were not very sensitive to changes in Sr abundances when these abundances were this low. The best estimate for an upper limit would be around  $[Sr/Fe] \sim 2.0$  for all stars, while the stars in the Milky Way halo in the sample of François et al. (2007) have  $-2.24 \lesssim [Sr/Fe] \lesssim 0.54$ . The upper limits for stars in Boötes are thus too high to yield any conclusions.

## 5.6 Yttrium

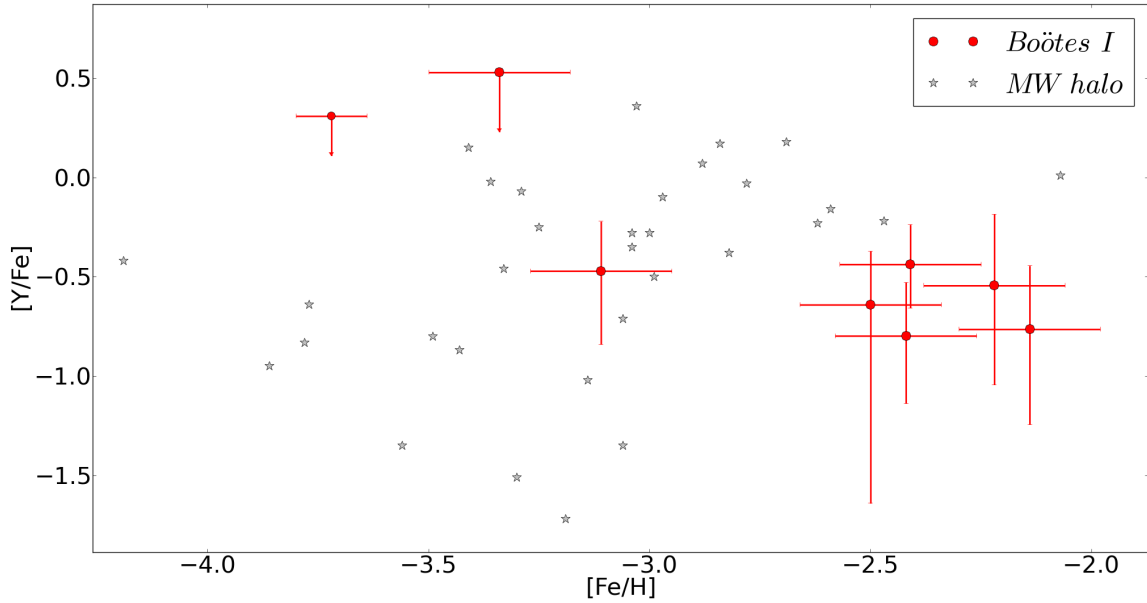


Figure 18:  $[Y/Fe]$  for stars in Boötes and the Milky Way halo (Cayrel et al. 2004, François et al. 2007). Symbols as in Fig. 14.

For Y, three lines have been used: those at 4854.9, 4883.7, 5087.4 Å. NY did not derive Y abundances, because these lines are very weak and noise makes it difficult to measure them as equivalent widths. Abundances are plotted in Fig. 18. For the two most metal-poor stars, only upper limits have been found. The other stars have  $[Y/Fe]$  close to each other.

## 5.7 Zirconium

There are three elements that belong to the first neutron capture peak, Sr, Y and Zr. Unfortunately, the four lines that could be used to determine Zr are very weak in all stars, resulting in relatively high upper limits on the abundances, as shown in Fig. 19. Upper limits of the three most metal-poor stars in Boötes are higher than the upperlimits for the five other stars. The brightest star, Boo94 and Boo1137, which was observed with UVES-slit setting should have relatively high S/N, but still give only a high upper limit.

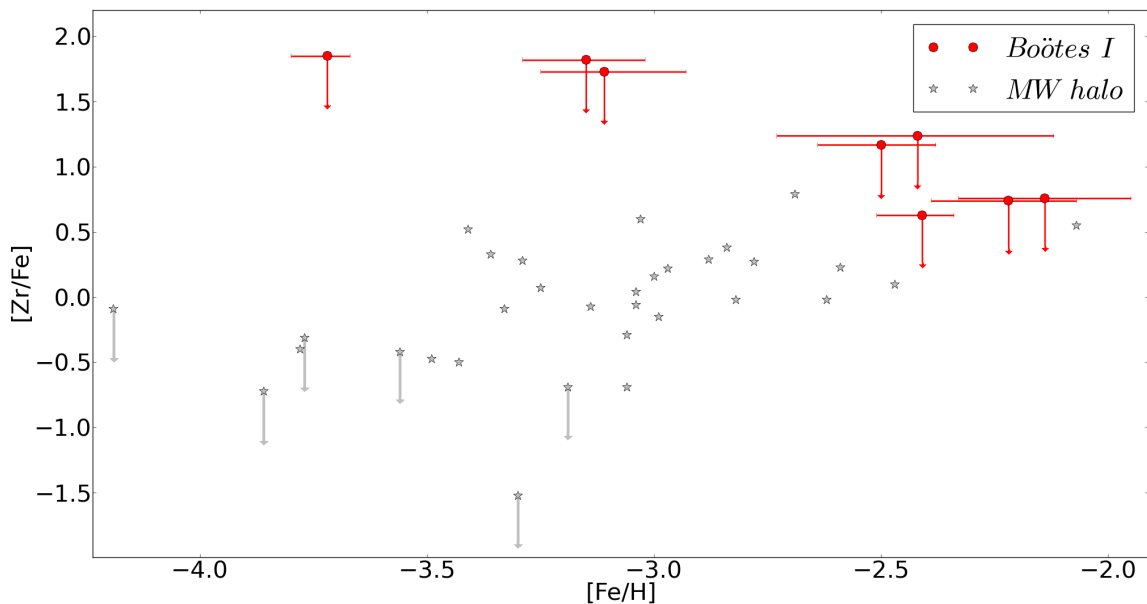


Figure 19:  $[Zr/Fe]$  for stars in *Boötes* and the Milky Way halo (Cayrel et al. 2004, François et al. 2007)

## 5.8 Errors

Errors were determined by looking which higher and lower abundances would still fit the absorption line when taking into account noise from the spectrum. In the case of Fe, an element with many lines, this was done for three lines: those at 4918.99, 5150.84 and 5383.38 Å. The chi-square of both the upper and lower limit was then calculated, as well as the chi-square of the best fit (this is always the lowest chi-square of the three). Upper and lower chi-squares are then divided by the best fit chi-square. The average of  $\chi_{upper}/\chi_{best}$  and  $\chi_{lower}/\chi_{best}$  was calculated. After this, finding upper and lower limits on the abundances for all 56 lines is a backwards process: instead of determining the chi-square for each model with different Fe abundance, the chi-square is the starting point. The model that corresponds best to this chi-square can now be found. It is important to notice that the upper and lower limits are usually not symmetric. The upper limit usually deviates less from the best fit than the lower limit does. This is especially true for weak lines, that can be hard to measure in the first place. In the end, the error analysis gives a list of lines, with upper and lower limits for the abundance of that line.

Some lines will of a given element have a smaller error than others and because of this, a weighted average should be used to calculate the average abundance of element X in the star. For this weighted average, the following formula was used:

$$\log \epsilon(X) = \frac{\sum_{i=1}^{N_X} \log \epsilon(X)_i \cdot w_i}{\sum_{i=1}^{N_X} w_i}$$

where  $w_i$  are the weights and the number of lines is  $N_X$ . The weight of line  $i$  is defined from the error that is in the abundance measurement of that line ( $\delta_{noise,i}$ ) as:

$$w_i = \frac{1}{\delta_{noise,i}^2}$$

Since the upper and lower error on a line are not the same, the average of both values was used for  $\delta_{noise,i}$ . The abundances together with their errors for all *Boötes* stars are given in Table 5.

Table 5: *Chemical abundances and errors for eight red giants in Boötes*

	<b>Boo33</b>	<b>Boo41</b>	<b>Boo94</b>	<b>Boo117</b>	<b>Boo119</b>	<b>Boo127</b>	<b>Boo130</b>	<b>Boo1137</b>
$\log \epsilon(\text{Fe})$	5.09	5.33	4.44	5.09	4.2	5.28	5.00	3.78
$[\text{Fe}/\text{H}]$	-2.41	-2.17	-3.06	-2.41	-3.3	-2.22	-2.5	-3.72
$\sigma[\text{Fe}/\text{H}]$	+0.26 -0.24	+0.5 -0.46	+0.09 -0.11	+0.35 -0.23	+0.15 -0.2	+0.64 -0.36	+0.27 -0.28	+0.05 -0.08
$\log \epsilon(\text{Mg})$	5.32	5.83	4.93	5.47	5.27	5.55	5.34	4.28
$[\text{Mg}/\text{Fe}]$	0.13	0.40	0.39	0.28	0.97	0.17	0.24	0.40
$\sigma[\text{Mg}/\text{Fe}]$	+0.13 -0.24	+0.23 -0.33	+0.17 -0.19	+0.14 -0.12	+0.26 -0.28	+0.22 -0.26	+0.14 -0.28	+0.05 -0.13
$\log \epsilon(\text{Zn})$	<2.25	2.54	0.41	2.5	<2.00	2.33	2.37	<1.35
$[\text{Zn}/\text{Fe}]$	<0.10	0.15	-1.09	0.35	<0.74	-0.01	0.31	<0.51
$\sigma[\text{Zn}/\text{Fe}]$	...	+0.29 -0.39	+0.20 -0.61	+0.10 -0.20	...	+0.22 -0.33	+0.21 -0.37	...
$\log \epsilon(\text{Y})$	-0.64	-0.69	-1.37	-1.01	<-0.6	-0.55	-0.93	<-1.2
$[\text{Y}/\text{Fe}]$	-0.44	-0.73	-0.52	-0.81	<0.89	-0.54	-0.64	<0.31
$\sigma[\text{Y}/\text{Fe}]$	+0.22 -0.29	+0.33 -0.62	+0.26 -0.50	+0.41 -0.28	...	+0.36 -0.52	+0.29 -1.08	...
$\log \epsilon(\text{Zr})$	<1.25	<1.2	<0.8	<1.25	<1.4	<1.1	<1.2	<1.25
$[\text{Zr}/\text{Fe}]$	<1.08	<0.79	<1.28	<1.08	<2.12	<0.74	<1.12	<1.14
$\sigma[\text{Zr}/\text{Fe}]$	...	...	...	...	...	...	...	...
$\log \epsilon(\text{Ba})$	-0.46	-0.02	-1.99	-0.26	-2.15	-0.14	-0.72	-2.26
$[\text{Ba}/\text{Fe}]$	-0.23	-0.03	-1.11	-0.03	-1.03	-0.1	-0.4	-0.72
$\sigma[\text{Ba}/\text{Fe}]$	+0.26 -0.24	+0.50 -0.46	+0.09 -0.11	+0.35 -0.23	+0.15 -0.20	+0.64 -0.36	+0.27 -0.28	+0.03 -0.06

## 6 Abundance patterns of stars in different environments

Chemical abundances of Fe, Mg and Ba have been measured and compared to the analysis from NY. Zn, Y and Zr have been measured too. A comparison of the abundances of these elements in Boötes and in Sculptor and the Milky Way halo can now be made. First, trends of individual elements will be compared and after that, the averaged abundances for different populations will be analysed. These comparisons may show whether the chemical evolution of the stars in the different environments has been similar or not.

### 6.1 Interpretation of elemental abundance ratios

The abundances of elements in RGB stars in Sculptor, the Milky Way halo and Boötes will be compared here. For all stars, the Fe abundances measured by synthetic spectra are used in the ratios  $[X/Fe]$  and  $[Fe/H]$  of the Boötes stars.

#### 6.1.1 Mg

Abundances derived for Mg by using synthetic spectra were compared to those determined by NY in the previous section. Mg is one of the  $\alpha$ -elements and because these elements are mostly formed in SN II, a decrease of  $[Mg/Fe]$  can be seen as SN Ia start to contribute.

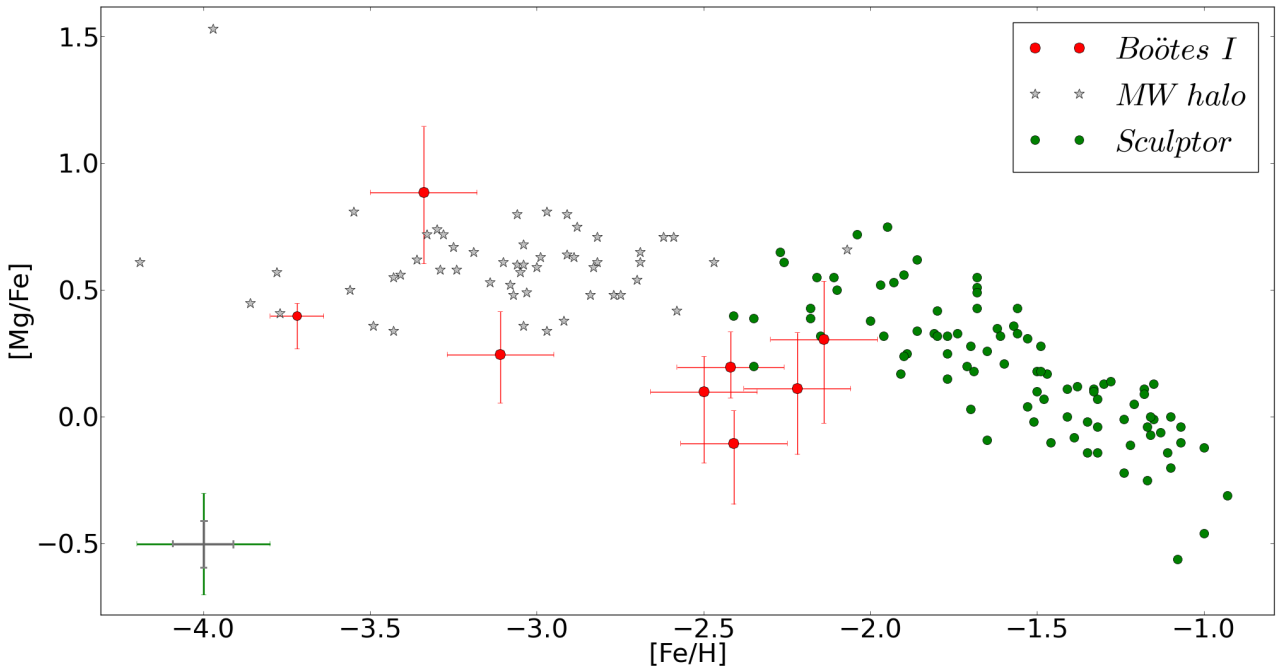


Figure 20:  $[Mg/Fe]$  for stars in Boötes (red dots), Sculptor (green dots, Hill et al. in prep) and the Milky Way halo (grey stars, Cayrel et al. 2004, Andrievsky et al. 2010). Typical errorbars for Sculptor (green) and the Milky Way halo (grey) are in the lower left corner.

Fig. 20 gives a comparison between  $[Mg/Fe]$  in different environments: RGB stars from the ultra-faint dSph Boötes, stars from the more massive Sculptor dSph and stars from the Galactic halo. In Sculptor,  $[Mg/Fe]$  decreases with increasing metallicity, meaning that SN Ia have occurred and enriched the material from which these stars formed. The RGB stars in the Milky Way halo show a fairly constant  $[Mg/Fe]$ . Mg abundances from Boötes stars do not show a decrease, but stay mostly constant, just as

stars from the Milky Way halo. However, their Mg abundances are lower than those in the Milky Way halo. Only Boo119, with  $[\text{Mg}/\text{Fe}] = +0.97$  is similar to the highest Mg abundances of halo stars. G13 also found high Mg for Boo119 and combining this with the high carbon abundance ( $[\text{C}/\text{Fe}] = +2.2$ , Lai et al. 2011), indicates that Boo119 is a CEMP star. Because of the low  $[\text{Ba}/\text{Fe}] = -1.0$  (NY analysis), they concluded that it is part of the CEMP-no subclass of CEMP stars (Beers & Christlieb, 2005). It is common for CEMP-no stars to also have enhanced Mg (Norris et al. 2013).

### 6.1.2 Ba

Ba is the result of the main  $s$ - and  $r$ -process, hence its origin is better understood than that of Y. It is in the second peak produced by the  $s$ -process, because it is a very stable nucleus. From the increase in  $[\text{Sr}, \text{Y}, \text{Zr}/\text{Ba}]$  with decreasing  $[\text{Fe}/\text{H}]$ , it is concluded by Travaglio et al. (2004) that production of Ba starts at a later time than that of Sr, Y and Zr. A delayed production for Ba can mean that it is produced in SNe of lower mass at these metallicities. Fig. 10 in François et al. (2007) shows that in halo stars  $[\text{Ba}/\text{Fe}]$  has a large scatter for  $-3.0 \leq [\text{Fe}/\text{H}] \leq -2.5$  and decreases at lower metallicity, reaching a value between  $\sim -2.0$  and  $-1.0$ . This increase in scatter and decline in  $[\text{Ba}/\text{Fe}]$  is also seen in dSphs, where it occurs at higher  $[\text{Fe}/\text{H}]$  (Tolstoy et al. 2009 and references therein). The large scatter is explained by Tolstoy et al. (2009) by concluding that the production of  $r$ -process elements happens in events that are less common to those where  $\alpha$ -elements are produced. Therefore,  $r$ -process abundances can be used as a better tracer of timescales and also as an indicator of enrichment processes.

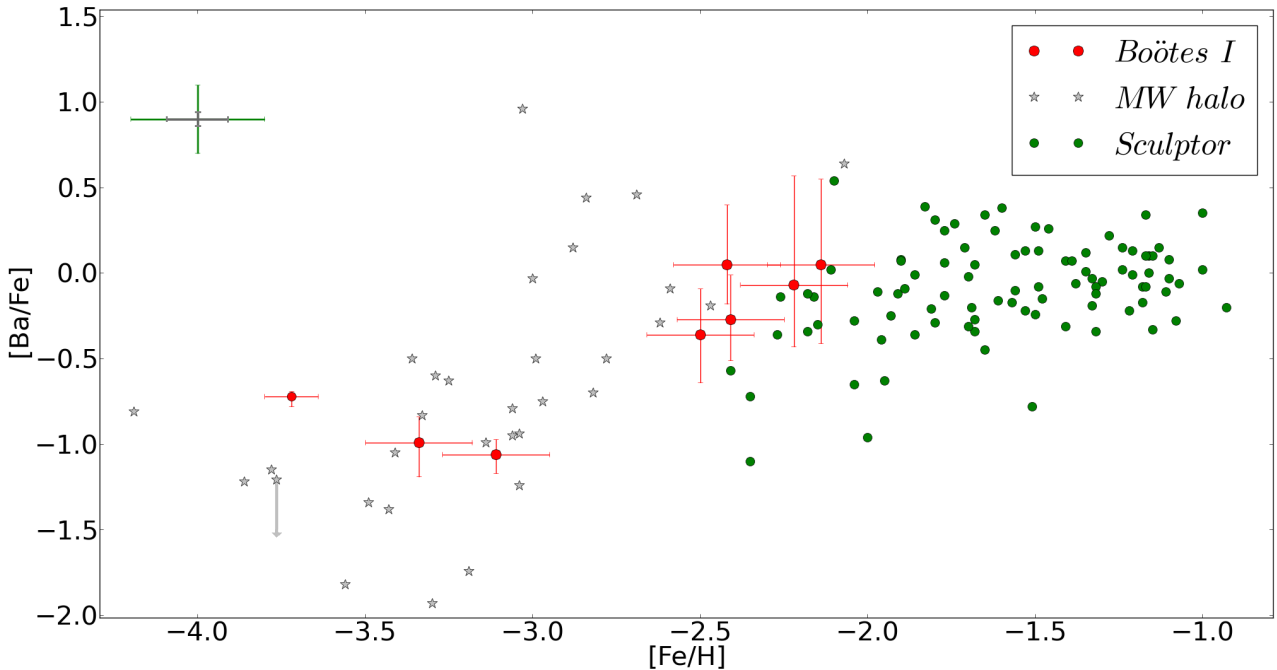


Figure 21:  $[\text{Ba}/\text{Fe}]$  for stars in Boötes, Sculptor (Hill et al. in prep) and the Milky Way halo (Cayrel et al. 2004, François et al. 2007). Symbols as in Fig. 20.

Fig. 21 gives  $[\text{Ba}/\text{Fe}]$  as function of  $[\text{Fe}/\text{H}]$ .  $[\text{Ba}/\text{Fe}]$  goes to lower values as  $[\text{Fe}/\text{H}]$  decreases for halo stars. For Sculptor however,  $[\text{Ba}/\text{Fe}]$  stays rather constant and starts to turn down for the lowest metallicity stars. Abundances in Boötes are consistent with those in the Milky Way and a downward trend is also observed. G13 conclude that the dispersion of  $[\text{Ba}/\text{Fe}]$  in Boötes is in agreement with that in the halo and this is also true for the abundances determined using synthetic spectra. Taking the ratio  $[\text{Ba}/\text{Fe}]$  reduces the difference between the two analyses to  $[\text{Ba}/\text{Fe}]_{\text{synthetic spectra}} - [\text{Ba}/\text{Fe}]_{\text{NY}} \approx -0.04$

dex. The conclusion would be the same for both analyses, namely that the stars in Boötes show  $[\text{Ba}/\text{Fe}]$  similar to that in halo stars.

### 6.1.3 Zn

While models like the one discussed in Iwamoto et al. (1999) suggest that Zn is not mainly produced in SN Ia and it does not follow Fe, exactly where it is formed is not clear. Umeda & Nomoto (2002) conclude that hypernovae are needed to explain the high Zn abundances at low  $[\text{Fe}/\text{H}]$ . The  $s$ -process for example predicts decreasing  $[\text{Zn}/\text{Fe}]$  as  $[\text{Fe}/\text{H}]$  increases, but it is seen that  $[\text{Zn}/\text{Fe}] \sim 0$  for  $-2.5 < [\text{Fe}/\text{H}] < 0$  and for lower metallicity,  $[\text{Fe}/\text{H}] < -2.5$ ,  $[\text{Zn}/\text{Fe}]$  increases. Similarly, they say that other production sites also cannot explain the behaviour of Zn. The solution they suggest are hypernovae, these are SNe that have high explosion energies. Two possible scenarios are suggested: SNe with relatively low mass ( $M \leq 13 M_{\odot}$ ) and explosion energy,  $E_{exp} \geq 2 \cdot 10^{51}$  erg, or high mass ( $M \geq 25 M_{\odot}$ ) SNe with  $E_{exp} \geq 10 \cdot 10^{51}$  erg. Both would produce little Fe and enough Zn, resulting in the required ratio of  $[\text{Zn}/\text{Fe}] \sim 0.5$  for  $[\text{Fe}/\text{H}] \leq -2.5$ . Umeda & Nomoto also concluded that pair instability supernovae cannot produce the high  $[\text{Zn}/\text{Fe}]$  ratio that is observed.

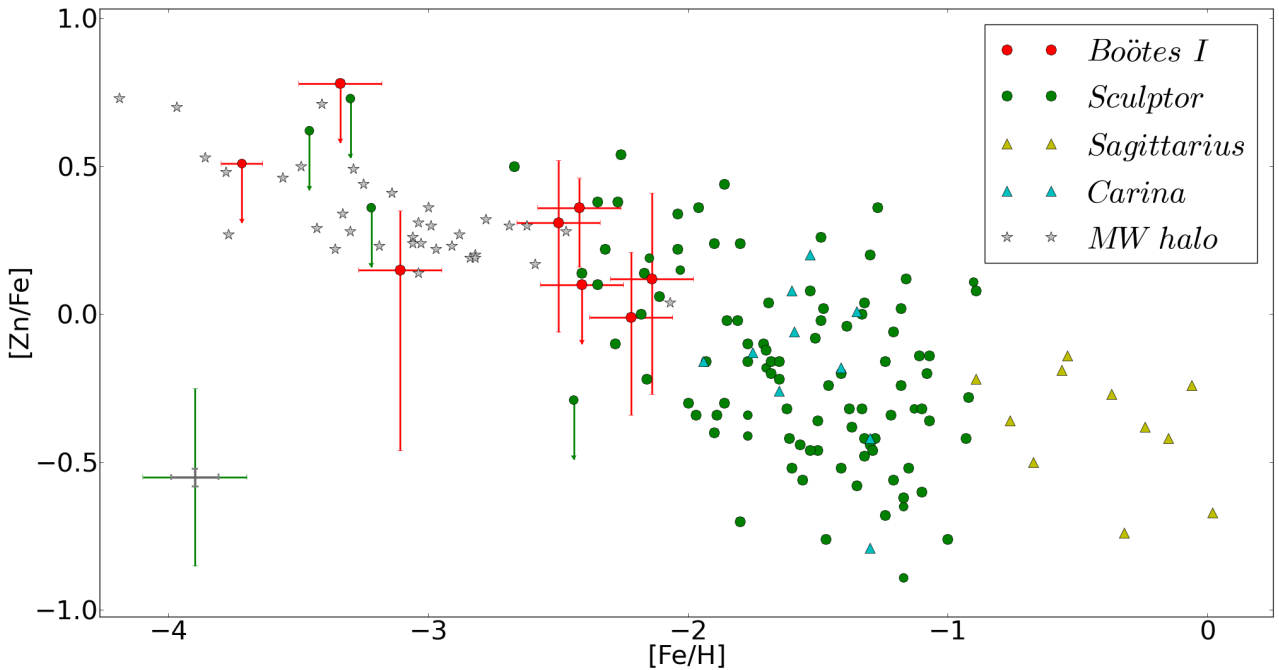


Figure 22:  $[\text{Zn}/\text{Fe}]$  for RGB stars in dSphs and in the Milky Way halo. The dSphs are: Boötes (this work), Sculptor (Shetrone et al. 2003, Geisler et al. 2005, Jablonka et al. 2015, Skúladóttir et al. 2016, Hill et al. in prep), Carina (cyan triangles, Shetrone et al. 2003, Venn et al. 2012) and Sagittarius (yellow triangles, Sbordone et al. 2007). Stars from the halo are from Cayrel et al. (2004) Symbols as in Fig. 20.

The abundances for the stars of Boötes can be found in Fig. 22. Zn abundances for several dSphs are also plotted, as well as stars from the Milky Way halo. For Sculptor, a downward trend of  $[\text{Zn}/\text{Fe}]$  with increasing  $[\text{Fe}/\text{H}]$  can be observed. There are not many data points from Carina and Sagittarius, but they seem to show the same behaviour as Sculptor. The Milky Way stars have a constant  $[\text{Zn}/\text{Fe}]$  for  $-3 \leq [\text{Fe}/\text{H}] \leq -0.5$ . The stars in Boötes are more similar to the Milky Way halo stars with the same metallicity than to the other dSphs,  $[\text{Zn}/\text{Fe}]$  does not seem to decrease with metallicity, but stays constant. This could be because  $[\text{Fe}/\text{H}]$  for the Boötes stars in this sample is not as high as for the stars

in Sculptor. In the region where  $[\text{Fe}/\text{H}]$  overlap for Boötes, Sculptor and the Milky Way halo,  $[\text{Zn}/\text{Fe}]$  are consistent in all three samples.

#### 6.1.4 Y

As was shortly explained in Section 2.3, the nucleosynthetic origin of Y is rather complicated. At solar metallicities, the  $s$ -process is the process that mainly contributes to Y, but at low metallicities, the  $r$ -process is most important, together with the LEPP or  $\nu\text{p}$ -process. A description of all these processes will be given here, to summarize what is known about the origin of elements from the first neutron capture peak.

The  $s$ -process takes place in environments where neutron densities are relatively low,  $n_n < 10^8 \text{ cm}^{-3}$ . Because of the low neutron densities, neutrons will be captured slowly, relative to  $\beta$  decay. This means that if it is possible for  $\beta$  decay to happen, it will happen before another neutron is captured. The  $s$ -process will thus make elements that are in the valley of  $\beta$  stability. There are three different components of the  $s$ -process distinguished at the moment: the main, the weak and the strong  $s$ -process (Busso et al. 1999). Of these, the main  $s$ -process is most important for Y and its neighbouring elements: Sr and Zr. According to the calculations of Travaglio et al. (2004) 69% of the solar Y abundance is produced by the main  $s$ -process and around 5% by the weak process. Stars on the asymptotic giant branch with  $M < 4 M_\odot$  are responsible for the main  $s$ -process. The  $s$ -process is found to be more effective for stars with lower metallicity (Gallino et al. 1998), but since low mass stars are most important for this process, they have not yet had enough time to contribute to the enrichment of the low metallicity stars in Boötes. The weak  $s$ -process contributes to the elements with atomic number up to  $\sim 90$  and takes place in massive stars, when they are at the end of their evolution. The strong  $s$ -process is most important for producing a large fraction of Pb.

In environments where the neutron density is much higher, the  $r$ -process can take place. Neutron capture is no longer a slow process that allows  $\beta$  decay, but happens fast enough to make isotopes that lie beyond the valley of  $\beta$  stability. The most likely site for this are core-collapse SNe, although it is not yet completely understood what the exact physical conditions are to produce the right amount of  $r$ -process elements (Thielemann et al. 2011). It was found by Travaglio et al. (2004) that about 18% of solar Y was missing and had to be produced by a process different from the standard  $r$ -process. They called this process the lighter element primary process (LEPP), because it should mainly contribute to the lighter neutron capture elements, Sr, Y and Zr. François et al. (2007) show that for  $-4.5 \leq [\text{Ba}/\text{H}] \leq -2.5$  the ratios  $[\text{Sr}, \text{Y}, \text{Zr}/\text{Ba}]$  increase as  $[\text{Ba}/\text{H}]$  decreases. Ba is part of the second peak produced by the  $r$ -process, while the other three elements belong to the first peak. This increase means that for stars at low metallicity, there has to be an additional process that contributes to the first peak, while it does not affect the second peak. For  $[\text{Ba}/\text{H}] \leq -4.5$  (corresponding to  $[\text{Fe}/\text{H}] \sim -3.0$ ), the  $[\text{Sr}, \text{Y}, \text{Zr}/\text{Ba}]$  ratios seem to be going to solar, just as they were at  $[\text{Ba}/\text{H}] \geq -2.5$ .

The LEPP process has also been called  $\nu\text{p}$ -process because it is assumed to occur in an environment where there are strong neutrino fluxes that cause the ejection of proton-rich matter (Thielemann et al. 2011). This could for example happen in the inner ejecta of SNe II, where the neutrino/antineutrino flux is large and antineutrinos will be captured mainly by protons, because of the high proton density. For a few seconds, the neutron density will become high enough,  $n_n = 10^4 - 10^5$ , for rapid neutron capture. Because of the neutron capture, it is possible for the nuclei to capture more protons, thus reaching  $A > 90$ . Sr, Y and Zr can easily be produced in this way and it depends on different parameters, such as the mass of the neutron star, whether heavier elements can be produced too.

Fig. 23, shows  $[\text{Y}/\text{Fe}]$  for Boötes together with abundances for some stars from Sculptor and the Milky Way halo.  $[\text{Y}/\text{Fe}]$  seems to stay constant in both Sculptor and Boötes, although there are not many stars for which Y abundances are measured. Halo stars show a large spread, larger than that in the dSphs, but that could be because there are more measurements.

Travaglio et al. (2004) conclude that in a comparison between the samples of stars in the Galactic disk and halo they used and their dSph sample,  $[\text{Y}/\text{Fe}]$  is a bit lower in dSph than in the Galactic stars.

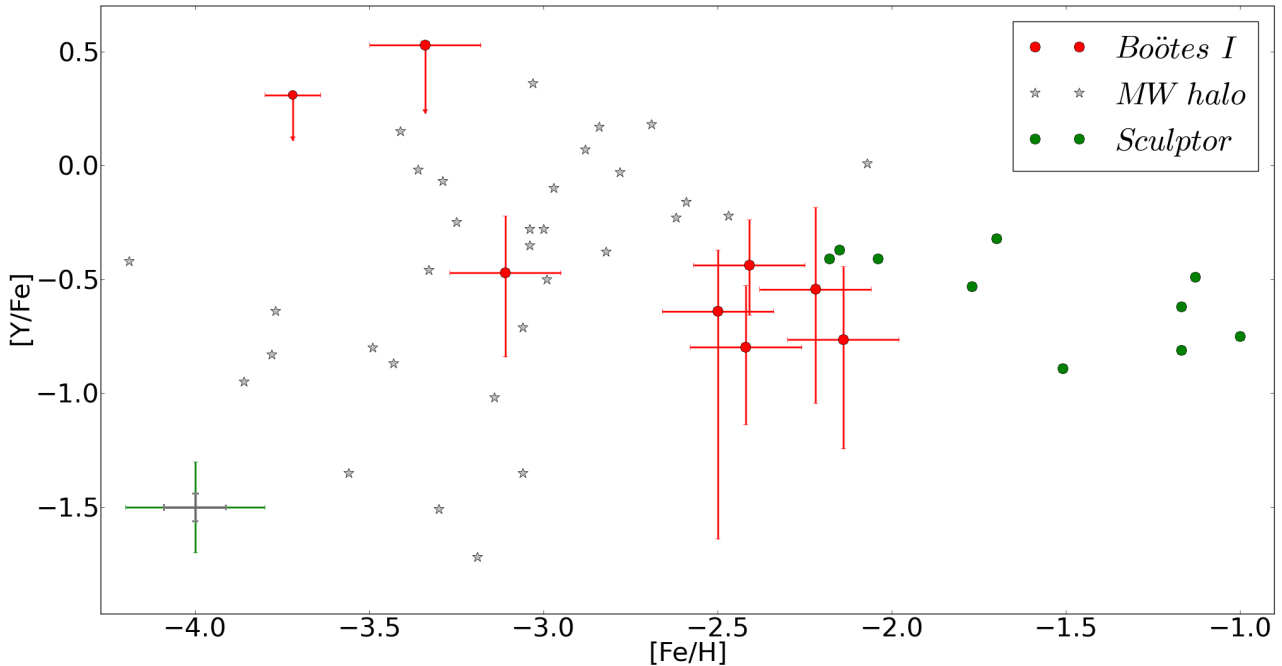


Figure 23:  $[Y/Fe]$  for stars in the dSphs Boötes and Sculptor (Hill et al. in prep) and in the Milky Way halo (Cayrel et al. 2004, François et al. 2007). Symbols as in Fig. 20.

They do not have data from dSphs with  $[Fe/H] \lesssim -2.1$ , so it is possible that at these low metallicities, stars from dSphs are similar to Milky Way halo stars, as seen in Fig. 23 for the stars in Boötes. The constant  $[Y/Fe]$  in Boötes, Sculptor and the Milky Way halo would suggest that Y is produced in SNe II that are present in all three environments. To keep  $[Y/Fe]$  constant as  $[Fe/H]$  increases, Y should be produced more at later times, otherwise a decrease would be seen just as for  $\alpha$ -elements. This can be due to the  $s$ -process, that is more important at higher  $[Fe/H]$ . For Boötes, this is not important, because of the low  $[Fe/H]$ .

In the context of the LEPP or  $\nu p$ -process, it is also interesting to look at the  $[Y/Ba]$  ratio that is plotted in Fig. 24. In all three stellar populations,  $[Y/Ba]$  is increasing towards lower  $[Ba/H]$ , meaning that  $[Y/Ba]$  is also increasing for lower metallicities. This means that in Boötes, an additional  $r$ -process is required, just as in the halo stars and in Sculptor. SNe type II have contributed to the enrichment of all three systems, so the  $\nu p$ -process could indeed occur in the inner ejecta of these SNe, as proposed by Thielemann et al. (2011).

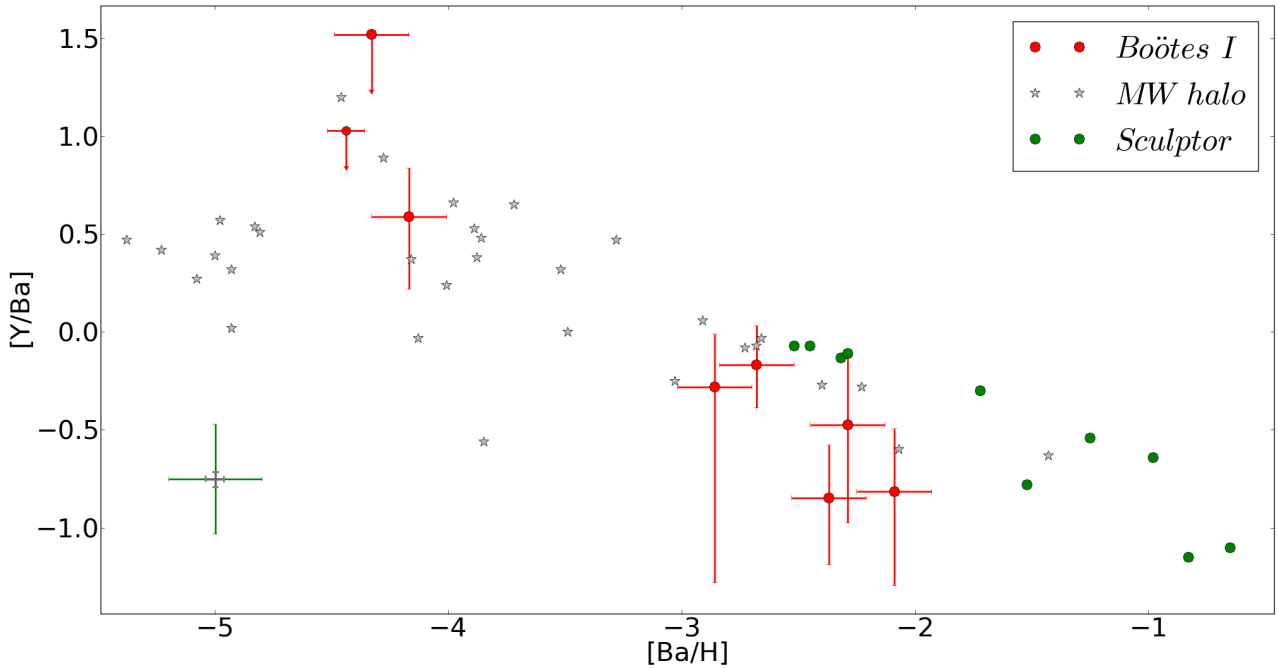


Figure 24:  $[Y/Ba]$  as function of  $[Ba/H]$  for stars in Boötes, Sculptor and Milky Way halo stars. References and symbols as in Fig. 23.

### 6.1.5 Zr

The origin of Zr is probably similar to that of Y, as was mentioned before. It is still interesting to also look at Zr, because there might be small differences in the production rates of Y and Zr and measuring abundances of more elements also helps to get a more complete understanding of the formation of neutron capture elements.

Fig. 25 is the same as Fig. 19, because there are no abundances of Zr for Sculptor. In Fig. 25, the upper limits of Zr for Boötes are shown together with abundances for the Milky Way halo. Halo stars may show an upward trend with increasing  $[Fe/H]$  in this range, but it is difficult to say this for sure, since there are not many stars. The upper limits for Boötes are relatively high upper limits, it is difficult to conclude anything from them. The upper limits for the most metal-rich stars in Boötes are at slightly higher  $[Zr/Fe]$  than the halo stars, so  $[Zr/Fe]$  cannot be much higher in Boötes than in the halo for these stars.

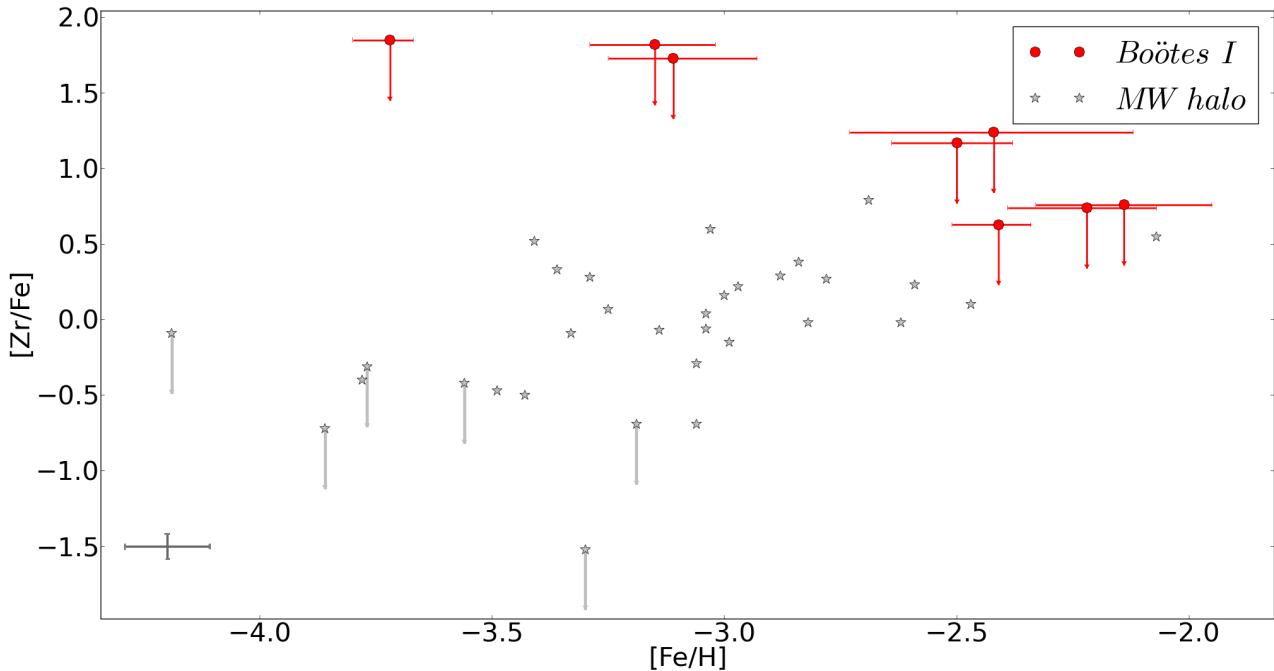


Figure 25:  $[Zr/Fe]$  for stars in Boötes and the Milky Way halo (Cayrel et al. 2004, François et al. 2007). Symbols as in Fig. 19.

## 6.2 Averaged abundance patterns

Previously, the measured chemical elements have been discussed separately but to get a more complete overview, it is interesting to look at all elemental abundances that have been measured. The abundances found for each element will be averaged for Boötes, Sculptor and the Milky Way halo to see what the similarities and differences are for these averaged abundances. The abundance patterns of single CEMP stars from different populations will also be compared to each other. In all of the samples, CEMP stars are taken out for the average, since their carbon-enhancement does not represent the average carbon abundances and they can be enhanced in e.g. Mg as well compared to the typical star. Abundances for Mg, Fe, Zn, Y, Zr and Ba are from this work, other elemental abundances are from NY. For abundances from NY, their average value for  $[Fe/H]$  ( $-2.54$ ) is used, this is  $0.1$  higher than  $[Fe/H]$  from this work. Errors are given by:  $error = \frac{\sigma}{\sqrt{N-1}}$ , where  $\sigma$  is the standard deviation and  $N$  is the number of stars that has measurements for that element.

### 6.2.1 Global abundance patterns

A comparison between Galactic halo stars and stars in Boötes gives the result in Fig. 26. The abundance patterns from both populations look very similar for most elements. When the difference in metallicity is ignored, Zn and Ba are the only elements that have a somewhat larger difference, but their abundances are still not extremely different. The conclusion from the previous section, that stars in Boötes are very similar to Galactic halo stars is strengthened here. Another sample of red giant stars from the halo is Yong et al. (2013) and the abundance pattern of this sample is also found to be very similar to that in Boötes, except for a lower  $[Fe/H]$ . The Ba abundance of Yong et al. is higher than in Cayrel et al. (2004), but comparable to Boötes within the errors.

For Sculptor, a subsample of 22 metal-poor stars within approximately the same metallicity range as the Cayrel et al. (2004) sample ( $-4.0 \leq [Fe/H] \leq -2.15$ ) was used, most stars are from the CaT survey

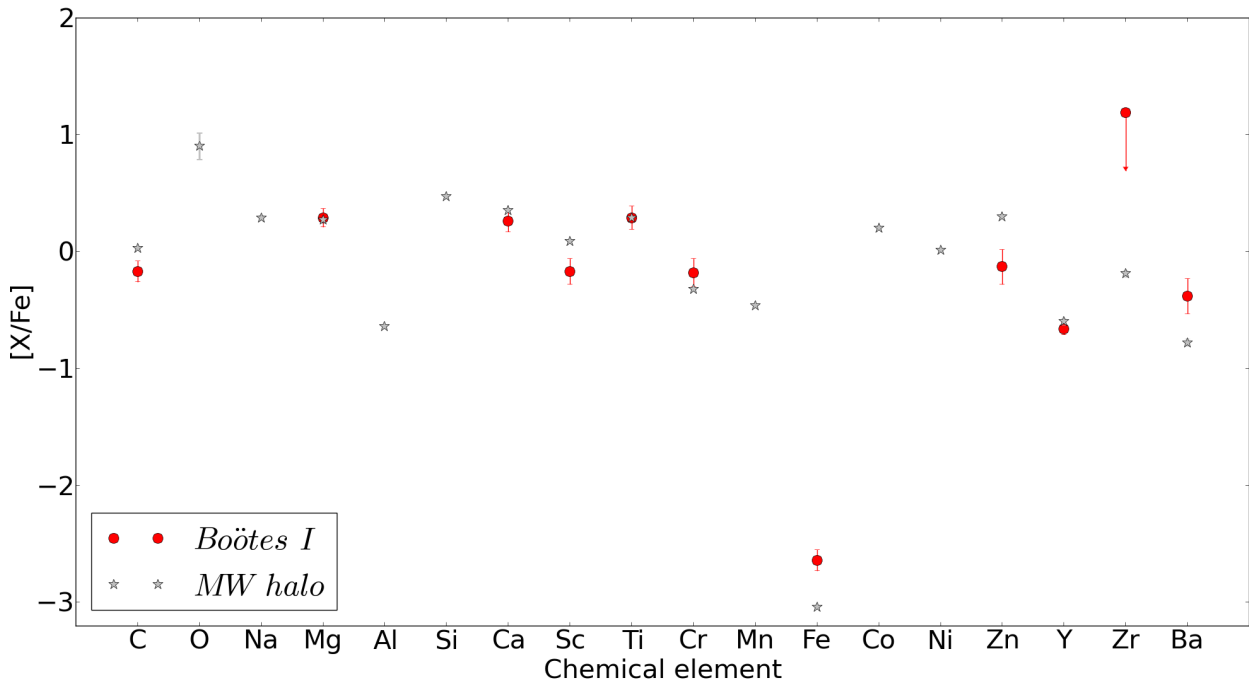


Figure 26: Abundance pattern for average abundances in Boötes (red dots) and in Galactic halo stars (grey stars, Cayrel et al. 2004). Element ratios  $[X/Fe]$  are plotted, except  $[Fe/H]$  for Fe.

(Tolstoy et al. 2004, Battaglia et al. 2008) and followed up by Tafelmeyer et al. 2010, Starkenburg et al. 2013, Simon et al. 2015, Jablonka et al. 2015., Skúladóttir et al. (2016), Hill et al. in prep. This is done to be able to make a more precise comparison between the samples. In Section 5, single stars were plotted and trends in their abundances with changing  $[Fe/H]$  were compared, but for comparing the abundances averaged over several stars,  $[Fe/H]$  should be comparable in the different samples. There is still a difference in metallicity for both samples, but this is less than it would be for the full Sculptor sample. In Fig. 27, the abundance patterns for Boötes, Milky Way halo and Sculptor are shown. While C abundances in Boötes and the halo were very similar, that in Sculptor is lower. There are only three stars in this sample from Sculptor that have a measurement for their C abundance, hence the large uncertainty. Within the errors, the difference between Sculptor and Boötes is negligible. The ratio  $[Sc/Fe]$  is higher in Sculptor than in Boötes, but similar to the halo. In the other elements, Sculptor is also similar to the halo and Boötes, its value for  $[Zn/Fe]$  for example is in-between that for halo stars and for Boötes.  $[Y/Fe]$  is just slightly higher in Sculptor. Y has only two measurements in Sculptor for this metallicity range, they are the two stars with lowest metallicity in Fig. 23, so this abundance may not be representative for Sculptor at these metallicities in general. If Y stays constant, as expected, other stars will have comparable abundances. For  $[Ba/Fe]$ , Boötes and Sculptor agree with each other.

## 6.2.2 Looking for hints of inhomogeneous mixing

The average of a number of stars was taken in the previous comparisons, but individual stars can show interesting patterns that may reflect inhomogeneous mixing. Dwarf galaxies like Boötes are probably enriched by the first stars and it is interesting to see if the ejecta of these stars was already well mixed or if some stars are clearly more enriched in certain elements than others, which would indicate inhomogeneous mixing. The first stars could also have produced distinct abundance patterns that may be seen in separate stars.

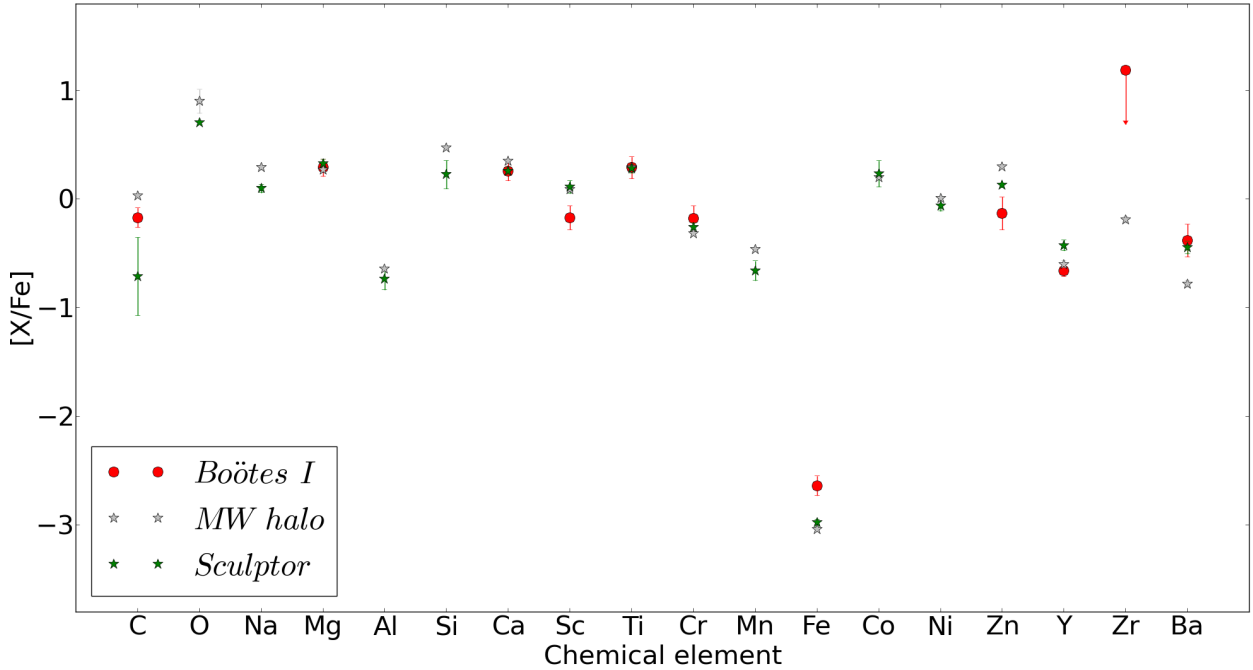


Figure 27: Abundance pattern for average abundances in Boötes and in Galactic halo stars (Cayrel et al. 2004) and Sculptor (green stars, only stars with  $-4.0 \leq [Fe/H] \leq -2.15$ , from Tafelmeyer et al. 2010, Starkenburg et al. 2013, Simon et al. 2015, Jablonka et al. 2015., Skúladóttir et al. 2016, Hill et al. in prep). Element ratios  $[X/Fe]$  are plotted, except  $[Fe/H]$  for Fe.

In Fig. 28 one star from Sculptor (ET0381) that was studied in Jablonka et al. (2015) is plotted together with the average of Boötes. There is only a minor difference in  $[Fe/H]$  (for Boötes, average  $[Fe/H] = -2.64$  and for ET0381, in Sculptor,  $[Fe/H] = -2.44$ ), but all other abundances are very different. The abundances in ET0381 are much lower than in Boötes. The low abundances of  $\alpha$ -elements were interpreted as due to inhomogeneous mixing for this star by Jablonka et al.: it could be missing the ejecta of the most massive SNe that enriched most of the other stars in Sculptor. This is also given as explanation for the low Zn values. For the stars in Jablonka et al. (2015),  $[Ba/Fe]$  in ET0381 is comparable to that in other stars in Sculptor, which they interpret as Ba being produced in medium mass SNe for these low metallicities. While  $[Ba/Fe]$  for Sculptor in Fig. 27 was similar to that in Boötes, there are 8 stars with only upper limits in that sample. Some of these are plotted in Fig. 13 from Jablonka et al. (2015) and they are around the same value of  $[Ba/Fe]$  as ET0381. Since Boötes is so dissimilar to ET0381, it is not likely that it is missing the ejecta from the more massive SNe.

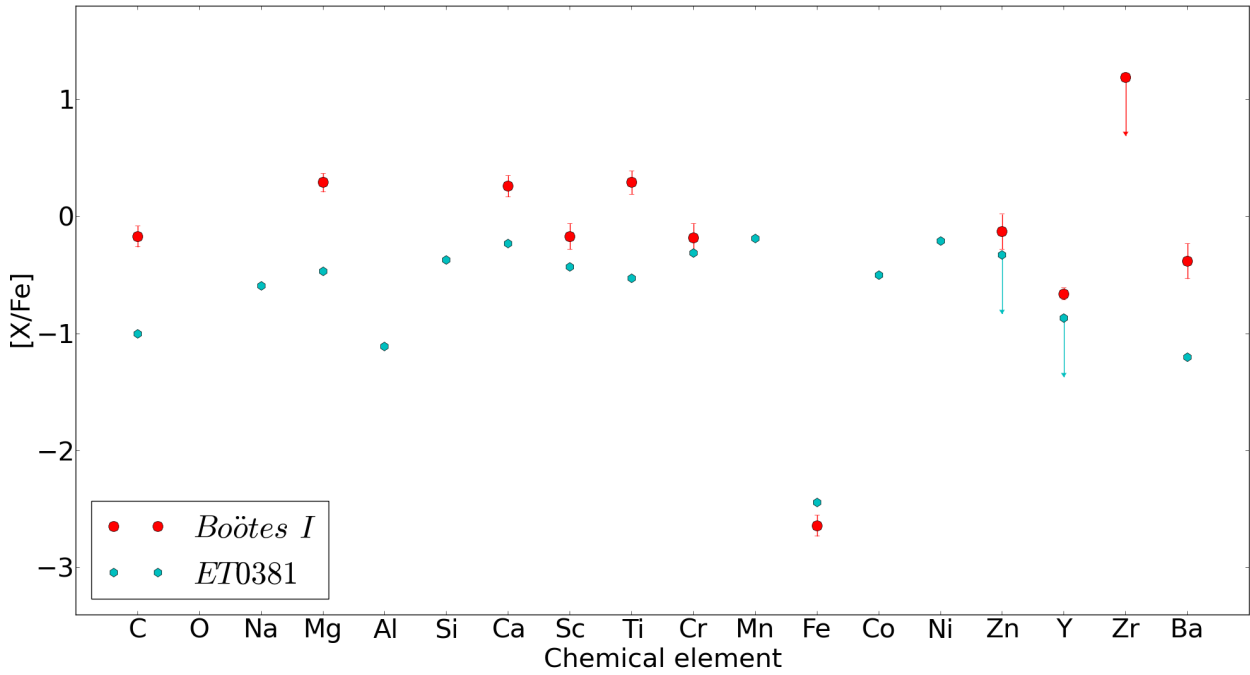


Figure 28: Abundance pattern for average abundances in Boötes and in ET0381 (cyan dots, Jablonka et al. 2015). Element ratios  $[X/Fe]$  are plotted, except for Fe it is  $[Fe/H]$

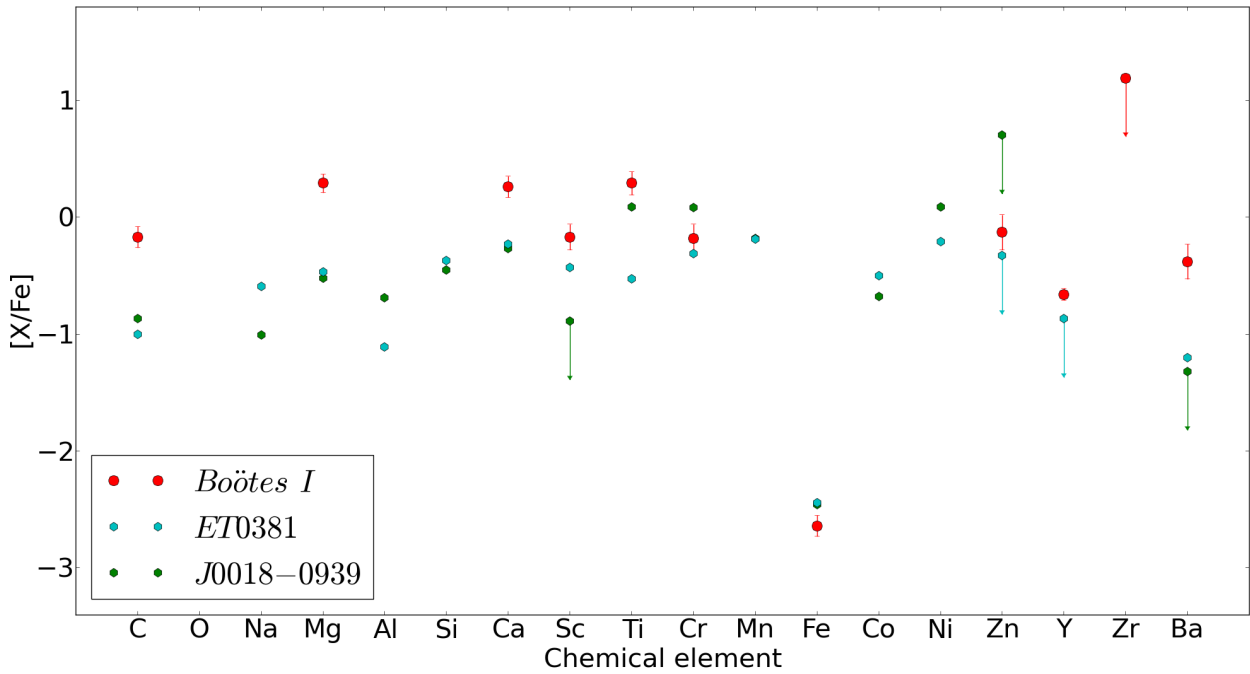


Figure 29: Abundance pattern for average abundances in Boötes, ET0381 (Jablonka et al. 2015) and J001820.5-093939.2 (green dots, Aoki et al. 2014). Element ratios  $[X/Fe]$  are plotted, except  $[Fe/H]$  for Fe.

Jablonka et al. remarked that the abundance pattern of ET0381 looks very similar to that of the star measured by Aoki et al. (2014), J001820.5-093939.2. Aoki et al. suggested that this pattern could be the result of a pair-instability supernova (PISN). Very massive stars with main sequence mass larger than  $100 M_{\odot}$  may end up as this type of SNe and since the first stars that formed in the Universe were probably very massive, the fingerprint of such a first star may have been found in J0081-0939. Jablonka et al. however reasoned that the high energy released by such an explosion would most likely have heated and blown away the gas in Sculptor, resulting in a reduced star formation rate in, or even the end of, star formation. Sculptor has quite a long star formation history however (de Boer et al. 2012), so Jablonka et al. suggest that ejecta of the most massive SNe are missing in J0081-0939, just as for ET0381. Fig. 29 does show that the two stars are more similar to each other than to Boötes, but for some elements, such as Al, the difference is still quite large. For Zn, Aoki et al. only have an upper limit that is higher than the abundance in Boötes and there is no measurement for Y. There is also only an upper limit for Ba, but this one is lower than  $[\text{Ba}/\text{Fe}]$  in Boötes and also slightly lower than  $[\text{Ba}/\text{Fe}]$  in ET0381.

From these comparisons, it is clear that the stars in Boötes are very similar to those in the Milky Way halo and also similar to stars with about the same metallicity in Sculptor. The average abundances of Boötes are not similar to abundances of the two unusual stars ET0381 and J001820. Both stars are probably missing ejecta of massive SNe and this indicates inhomogeneous mixing. The high Ti value found by G13 for Boo41 may indicate signs of inhomogeneous mixing, but all the other abundances of this star are similar to those in the other stars of Boötes. The effect of outliers in the Boötes sample is small, as can be seen from the small abundance dispersions. There are not many stars that show outliers, except Boo41, but this is only a small sample. Although there may be signs that the interstellar medium (ISM) in Boötes was not completely mixed in some places, there are no stars that show the same pattern as ET0381 and J0081-0939.

### 6.2.3 Abundance patterns and star formation histories

Although the abundance patterns of Boötes and Sculptor may look similar, their star formation histories are different. The stars in Boötes formed in a very short period: Brown et al. (2014) show with an HST colour-magnitude diagram that stellar populations that are 13.4 – 13.3 Gyr old fit all the stars. With two populations that are so close to each other in age, this is also consistent with star formation occurring in a single burst. If Boötes has formed its stars in such a short period, SNe Ia will not have had time to contribute to the enrichment. For Sculptor, SNe Ia did contribute as can be seen from the decreasing  $[\alpha/\text{Fe}]$  ratios as function of  $[\text{Fe}/\text{H}]$ . Most of the stars in Sculptor have ages  $>10$  Gyr, but stars formed for a period of 6 – 7 Gyr (de Boer et al. 2012). The star formation started about 14 Gyr ago and lasted to approximately 7 Gyr ago, but with a rapidly decreasing rate. This is very different from what is seen in Boötes and this difference in star formation history can be seen in abundances at higher metallicities. For the subsample of metal-poor Sculptor stars, abundances look similar to those in Boötes.

### 6.2.4 Comparison to CEMP-no stars

The final comparison will be between a CEMP-no star in Boötes and one in Sculptor. These stars may be enhanced by only primordial SNe (Beers & Christlieb, 2005) and their abundances may therefore reflect properties of the first stars.

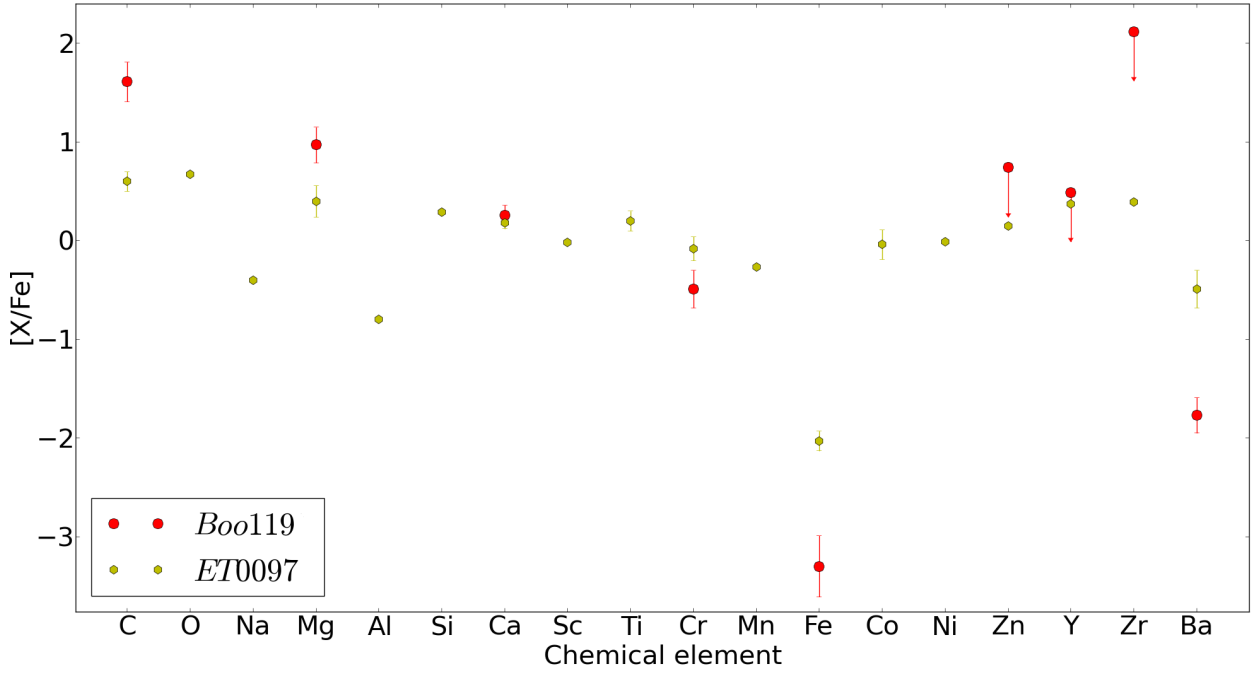


Figure 30: Abundance pattern for *Boo119* (red dots) and *ET0097* (yellow dots, Skúladóttir et al. 2015). Element ratios  $[X/Fe]$  are plotted, except  $[Fe/H]$  for Fe.

In Fig. 30 two CEMP-no stars, ET0097 from Sculptor and Boo119, are shown. Because Boo119 is enhanced in Mg and ET0097 is not, all abundance ratios  $[X/Mg]$  will be affected by the enhanced Mg in Boötes, so abundance ratios  $[X/Fe]$  are plotted, despite the very different metallicities of the stars. ET0097 is the first CEMP star that was discovered in Sculptor (Skúladóttir et al. 2015). The ratio  $[C/Fe]$  is lower in ET0097, but  $\log \epsilon(C)_{ET0097} = 7.0$ , a bit higher than the values for Boo119,  $\log \epsilon(C)_{Boo119} = 6.83$ , thus the absolute C abundances are almost the same. From these two stars, it seems like C abundance in CEMP-no stars does not change with  $[Fe/H]$ .  $[Ca/Fe]$  is approximately the same in both stars, but  $[Cr/Fe]$  and  $[Ba/Fe]$  are both lower in Boo119 than in ET0097, although the difference for  $[Cr/Fe]$  is very small when the errors are taken into account. As could be seen in Fig. 21,  $[Ba/Fe]$  decreases in stars of lower metallicity. Since  $[Fe/H]$  in Boo119 is lower than in ET0097, both probably show normal behaviour for  $[Ba/Fe]$ . For Zn, Y and Zr, there are only upper limits for Boo119. All of these limits are above the abundances measured by Skúladóttir et al. (2015), making it difficult to draw a conclusion from this. Abundance ratios for the few elements that could be measured in Boo119 are similar to those in ET0097, except for Fe and Ba. More elemental abundances need to be measured to be able to make a better conclusion.

## 7 Primordial SNe in Boötes

This last section will discuss what the properties of primordial SNe were that could have enriched Boötes. This has not been done before for Boötes, although it is possible that this dwarf galaxy has only been enriched by primordial SNe. It could give more information about the first SNe and their role in chemical evolution. G13 already concluded that Boötes is a self-enriching system. No enrichment from other systems is needed to explain the measured abundances and because Boötes is a very old system that probably formed before the epoch of reionization, it has evolved from almost primordial abundances. The first stars that formed from this primordial mix of gas, also called Population III stars, were metal-free stars and the imprint they left may be found in the eight stars from Boötes that have been analysed.

### 7.1 Starfit

To find out more about those first SNe, the online fitting program Starfit<sup>5</sup> (Heger & Woosley, 2010, Chan et al. in prep) was used. Heger & Woosley discuss the evolution of metal-free stars using the KEPLER code (Weaver et al. 1978, Woosley et al. 2002). This code was developed to study the different phases of stellar evolution, including explosive nucleosynthesis. Essentially, Starfit calculates what the mass, explosion energy and amount of mixing should be in a single or in multiple SNe to give the elemental yields that correspond to observed abundances. Elemental abundances should be given as input and a model database can be chosen.

One of the differences between the model databases is related to the modelling of the explosion. This is done by giving all mass outside a certain radius momentum, blowing the gas away. Heger & Woosley call this a piston model, since it is similar to a piston that pushes away everything that is on the other side of it. The piston can be placed at different positions, this affects the explosion energy and thus the amount of matter that is ejected. One possible position is at the edge of the iron core and another one is where the stellar density starts to decline rapidly. This is also where the oxygen shell begins. It is called the  $S = 4$  model, because the entropy per baryon,  $S/N_A k_B = 4.0$ . For the iron core placement models only two possible explosion energies are possible: 1.2 and 10 Bethe (1 B =  $10^{51}$  erg), while for the second placement, there are ten possible explosion energies ranging from 0.3 to 10.0 B. Apart from piston placement, the range of masses spanned by the models can be chosen. There are two possibilities: from 10–100  $M_\odot$  (used in Heger & Woosley, 2010) and from 9.6–100  $M_\odot$ , an update to the previous paper. This gives four possible databases.

One of the other parameters concerns the combination of elements. This means combining C and N to CN or C, N and O to CNO. Because there are no N abundances available for the Boötes sample, this is not important for Boötes, but combining C and N can significantly improve some fits for the halo sample of Cayrel et al. (2014) (Heger & Woosley, 2010).

The model database with piston at  $S = 4$  and for stellar mass range 9.6–100  $M_\odot$  was chosen here, because this database has the most models. Asplund et al. (2009) was chosen as reference for solar abundances. Both fits for a single SN and for up to three SNe were made. An important difference between the programs for single and multiple SNe is that the best fitting model is found for the single one and there is a limited calculation time for fitting multiple SNe. The result is that multiple SNe cases can differ each time, since the order of the models that are fit to the data can change and there are multiple combinations that can give a good fit. In the setting for multiple SNe, the first SN is one that fits most abundances relatively well, the residual is then fitted by another one, etc. until the number of SNe given as input is reached.

### 7.2 Results

Not only abundances in Boötes were fitted by the Starfit models, abundances from Sculptor and the Milky Way halo were also used to compare the results. The results from these primordial SNe models

---

<sup>5</sup><http://starfit.org/>

can be combined with the results from the abundances derived before to give a more complete overview of the chemical enrichment in different environments.

### 7.2.1 Starfit for Boötes

Table 6: Average abundances for Boötes used in Starfit

Element	$\log \epsilon(X)$	Error
C	5.72	0.09
Fe	4.86	0.09
Mg	5.25	0.08
Ca	4.06	0.09
Sc	0.44	0.11
Ti	2.71	0.10
Cr	2.92	0.12
Zn	1.96	0.15
Y	-0.91	0.05
Zr	1.03	-0.30
Ba	-0.84	0.15

First, the average abundance pattern in Boötes was fitted. Boo119 was excluded from the sample, because it is carbon-enhanced. Eleven elemental abundances are provided, six of which come from measurements done in this project, the other five are from NY. Errors are calculated by using  $error = \frac{\sigma}{N-1}$ , just as in the previous section. The values used as input for Starfit are in Table 6. A negative error means that there is only an upper limit for that element. Only Zr has this, other upper limits are taken out (e.g. Y in Boo1137), because they are quite high and would have a large effect on the average abundance. For the fitting of multiple SNe, a calculation time of 5 seconds was used. Taking a longer calculation time did not significantly change the results.

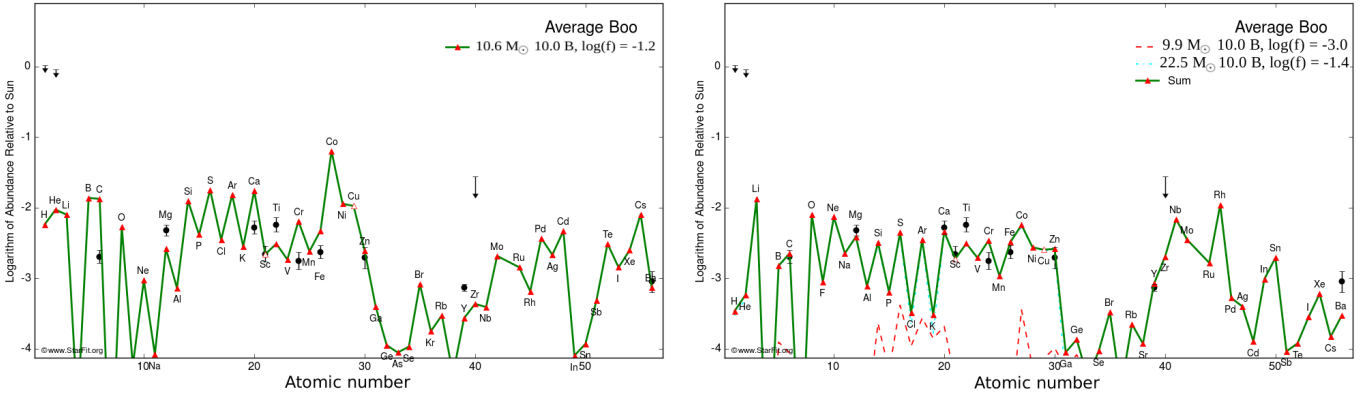


Figure 31: *Left: Single SN fit to average abundances in Boötes,  $\chi = 22.2$ . Right: Two SNe fitted to average abundances in Boötes,  $\chi = 2.7$ . Measurements are black dots, the solid green line with red triangles shows the total abundances produced by SNe, while contributions of single SNe are dashed or dotted lines. Open triangles are lower limits on produced abundances. Mass, explosion energy and mixing of each SN are given on the top right.*

In Figs. 31 and 32 the Starfit results for the average abundances in Boötes are shown. The left panel of Fig. 31 shows that a single SN does not give a good fit to several abundances in Boötes, including Mg and Ba. By adding a second one, the fit gets much better:  $\chi^2$  goes from 22.2 to 2.7. The right plot in Fig. 32 gives the best fit,  $\chi^2 = 1.7$ , this is for three SNe.

If abundances would have been produced by a single SN, it would have been one with a low mass, but

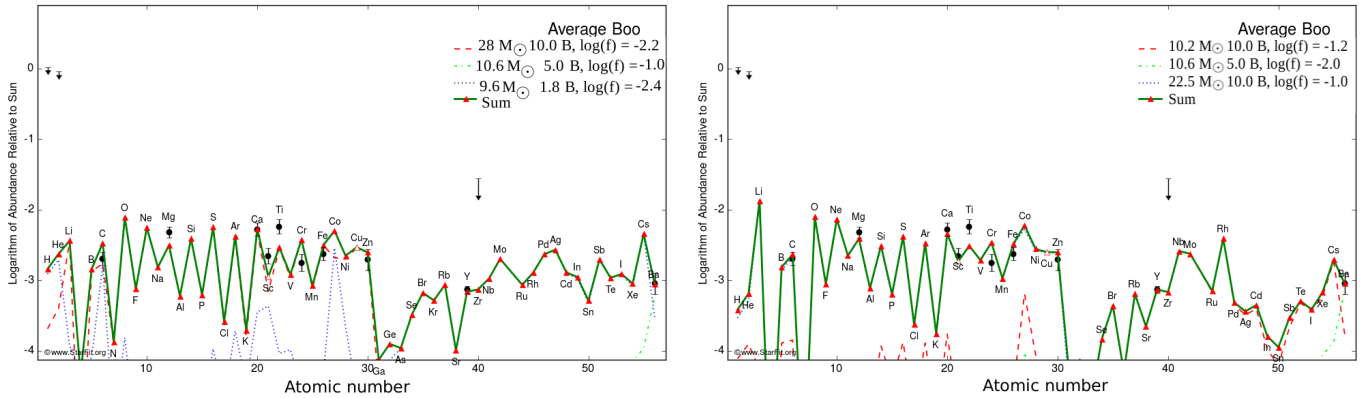


Figure 32: *Left:* Three SNe fitted to average abundances in Boötes,  $\chi^2 = 2.8$ . *Right:* Three SNe fitted to average abundances in Boötes,  $\chi^2 = 1.7$ . See Fig. 31 for description of symbols.

high explosion energy. For the fits with two and three SNe, one of those SN had larger mass,  $M > 20 M_{\odot}$ . Explosion energies are still quite high, but it is interesting to see that lower explosion energies are possible in the fit from the left panel of Fig. 32. This is also the fit that had the most massive ( $M = 28 M_{\odot}$ ) SN. The two panels of that same figure show that, despite using the same parameters, the fitting results can change. This was most evident for three SNe or more. In most cases, Zn and Y are fitted well. Omitting these two elements leads to results with SNe in a larger mass range, up to  $M \sim 40 M_{\odot}$ . Including Zn and Y thus has the effect of constraining the masses of zero-metallicity SNe that could have enriched Boötes. In general, it is possible to say that zero-metallicity SNe of low-mass and high explosion energy are needed to explain the abundance pattern in Boötes.

## 7.2.2 Starfit for the Milky Way halo

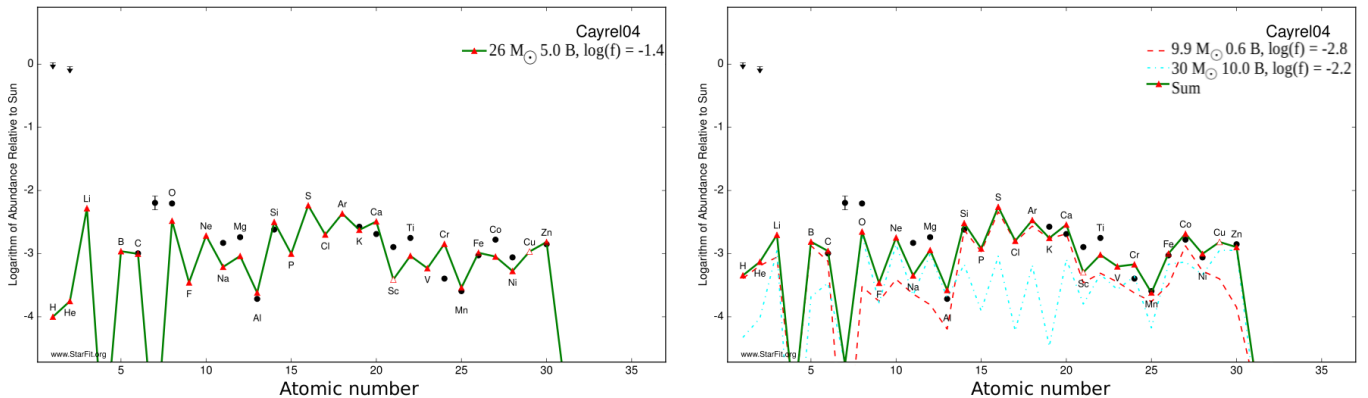


Figure 33: *Left:* Single SN fit to average abundances in Galactic halo (Cayrel et al. 2004),  $\chi^2 = 458.2$ . *Right:* Two SNe fitted to average abundances in Galactic halo,  $\chi^2 = 236.9$ . See Fig. 31 for description of symbols.

A comparison between these results and results for the Milky Way halo can be made. The halo stars from Cayrel et al. (2004) were fitted with the Starfit models in Heger & Woosley (2010) and there it was found that the best fits were given for low mass ( $M = 11\text{--}15 M_{\odot}$ ), low explosion energy SNe. Combining C and N also gave a better fit. In this paper, an IMF fit was made, which is different from the fits done here. The SNe models are the same, but with the online fitting tool used here, it is not possible to change the IMF and therefore no specific mass range of models can be selected either.

When Starfit is used with the Cayrel et al. abundances, a single SN fit has  $\chi^2 = 458.2$ , so it does not give a good fit either, as seen in the left panel of Fig. 33. The right panel of this figure shows that using two SNe increases the goodness of the fit, but the  $\chi^2 = 236.9$ , which is still not good. With more SNe, the fit does not get much better. A single SN would have  $M = 26 M_\odot$  and explosion energy of 5.0 B. The fit for two SNe has one of very low mass,  $M = 9.9 M_\odot$  and one with a slightly higher mass,  $M = 30 M_\odot$ . For three, masses differ quite a lot, usually one has  $M \sim 10 M_\odot$  and two are more massive. These higher masses are typically around 30–40  $M_\odot$ , but masses as high as 60  $M_\odot$  occur sporadically. In this sample of stars the masses of the stars exploding as SNe are on average a bit higher than for Boötes.

For the sample of halo red giants from Yong et al. (2013), Starfit also indicate SNe that on average have higher mass than in Boötes. This sample has stars with  $[\text{Fe}/\text{H}] \leq -3.5$  and is more metal-poor on average than Boötes. The best fitting individual SN would have  $M = 22.5 M_\odot$  and explosion energy of 10.0 B. Multiple SNe can have a range of masses that is similar to that for Cayrel et al. (2004), although masses as high as 60  $M_\odot$  have not been found. All the fits have large  $\chi^2$  values,  $400 \lesssim \chi^2 \lesssim 580$ , thus neither of the fits is very good.

For both Milky Way halo star samples, SNe with masses larger than 30  $M_\odot$  occur more often than in Boötes. This might be because the halo is much larger than in Boötes and so there are simply more massive stars. The fact that none of the fits for the halo stars is as good as the fit for Boötes, may indicate that the assumption that halo stars are only enriched by primordial SNe is not valid.

### 7.2.3 Starfit for Sculptor

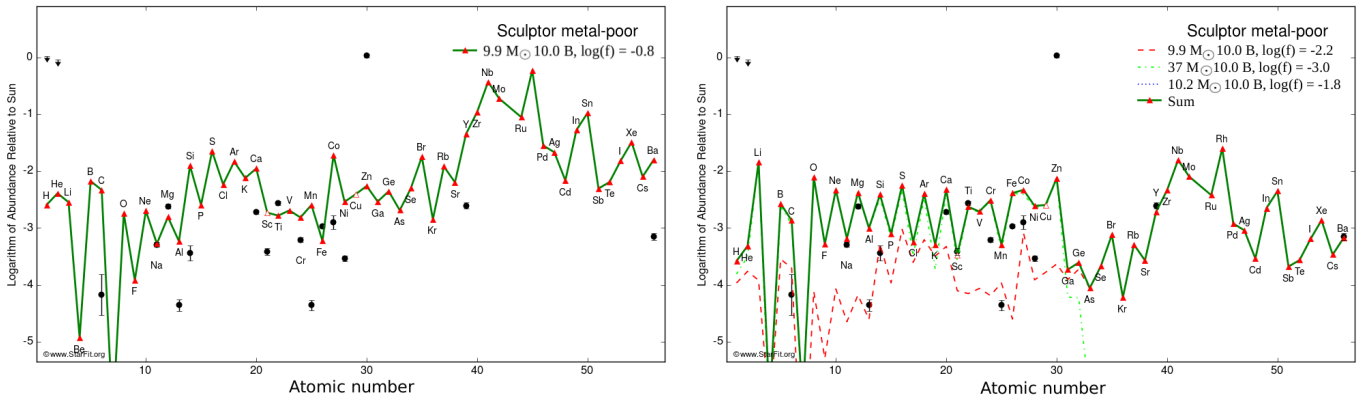


Figure 34: *Left: Single SN fit to average abundances in Sculptor,  $\chi^2 = 571.4$ . Right: Three SNe fitted to average abundances in Sculptor,  $\chi^2 = 425.8$ . See Fig. 31 for description of symbols.*

In the metal-poor sample of stars from Sculptor, a single SNe does not give a good fit ( $\chi^2 = 571.4$ ), but it would also be of low mass, as seen in the left panel of Fig. 34. More massive SNe give a somewhat better fit,  $\chi^2 = 425.8$ , if they can be combined with low mass ones as shown in Fig. 34, the right panel, that shows the fit of three SNe. Having a SNe with  $M \sim 35 M_\odot$  is not unusual for this metal-poor sample of Sculptor. The range over which mass changes is not as large as in the halo however. It can be seen that none of the fits is particularly good for these stars, probably because using only zero-metallicity SNe is not a good assumption for Sculptor as it has been forming stars over a more extended period than Boötes.

### 7.2.4 Starfit for single stars

Starfit was used too for the CEMP-no star in Sculptor, ET0097 (Skúladóttir et al. 2015) and also the unusual star ET0381 (Jablonka et al. 2015). For both, the best fit for a single SN is one of low mass,  $M \sim 10 M_\odot$ , with  $\chi^2$  values of 25 and 55 respectively. Fits are better for multiple SNe, reaching  $\chi^2 \lesssim 10$

for two or more SNe. Especially ET0097, the CEMP-no star has good fits:  $\chi^2 \sim 2 - 3$  for two or three SNe. For ET0381, the masses for multiple SNe are still low, in the same range as for the metal-poor Sculptor sample. When multiple SNe are fitted to ET0097, one of them can be of higher mass,  $M \sim 30-90 M_{\odot}$ .

ET0381, with  $[\text{Fe}/\text{H}] = -2.44$ , is in the same range of  $[\text{Fe}/\text{H}]$  that was used for the subsample of Sculptor, so the result that SNe are of similar mass is not unexpected. The interesting abundance pattern that this star showed could thus be the result of SNe with low-mass progenitors. ET0097 has  $[\text{Fe}/\text{H}] = -2.03$ , a bit higher than the metal-poor subsample. A SNe from a progenitor with a mass of  $90 M_{\odot}$  is significantly different from the low-mass SNe that were needed in the other Sculptor stars. This star is fitted very well by the primordial SNe, so it may be that it is indeed only enriched by these SNe. The high C abundance might be the reason for the high SN mass.

## 8 Discussion

### 8.1 Zn, Y and Zr

As could be seen in Fig. 22, Zn abundances in Boötes are most similar to those in the Galactic halo. In Boötes and the halo,  $[\text{Zn}/\text{Fe}]$  stays more or less constant, but in Sculptor, which has higher  $[\text{Fe}/\text{H}]$ , the ratio decreases with increasing  $[\text{Fe}/\text{H}]$ . The  $\alpha$ -like behaviour of Zn would suggest that the nucleosynthetic origin of this element is the same as that of the  $\alpha$ -elements, so SNe II would be important. As was already discussed in Section 5.4, it is not as simple as it seems. Umeda & Nomoto (2002) show that hypernovae are needed to get the observed Zn abundances at low metallicity. The combination of SN II and hypernovae would also be needed for Boötes, because of its similarity to the Milky Way halo.

In the comparison for Zn, two other dSphs, Carina and Sagittarius were also included to see if Boötes was more similar to them. Fig. 22 shows that Carina behaves similar to Sculptor and also has the same  $[\text{Fe}/\text{H}]$ . Another dSph, Sagittarius, is at higher  $[\text{Fe}/\text{H}]$  and also shows a decline of  $[\text{Zn}/\text{Fe}]$ . These three dSphs with higher mass have stars at higher metallicities meaning their star formation continued for a longer time and/or they could have been enriched faster than Boötes. Sculptor, Carina and Sagittarius are more similar to each other than to Boötes.

That the stars from Boötes are more similar to the Milky Way halo than to other dSphs differs from the conclusion from Ishigaki et al. (2014). While Ishigaki et al. concluded that  $[\text{Mg}/\text{Fe}]$  in Boötes was more similar to that in more luminous dSphs than in the halo, Fig. 20 seems to show that although  $[\text{Mg}/\text{Fe}]$  in Boötes is lower than in the Milky Way halo, the decreasing trend that is seen in Sculptor is not observed in Boötes. Ishigaki et al. concluded that  $[\text{Mg}/\text{Fe}]$  and  $[\text{Ba}/\text{H}]$  in Boötes are more similar to the more luminous dSphs than to other ultra-faint ones. There are only a few stars for each dSph in their Figs. 10 and 12 and they do not have a comparison with Sculptor. Since the ultra-faint dwarfs on average have  $[\text{Mg}/\text{Fe}]$  higher than the Milky Way halo stars, Boötes would indeed not be similar to those small galaxies. The main reason that Ishigaki et al. find Boötes to be more similar to classical dSphs, while this work concludes that Boötes looks more similar to the halo, is probably that Ishigaki et al. look at dSphs at lower metallicity than Sculptor. These dSphs are not used in this work. The conclusion would thus be that Boötes is most similar to the Milky Way halo and to stars with  $[\text{Fe}/\text{H}] \lesssim -2$  in Sculptor.

There is probably a  $\nu\text{p}$ -process at low metallicity that produces elements from the first neutron capture peak, like Y, but does not contribute to the formation of Ba. This is concluded from the increase of  $[\text{Y}/\text{Ba}]$  with decreasing  $[\text{Ba}/\text{Fe}]$  (e.g. François et al. 2007), a trend that can also be seen in Fig. 24 for Boötes. It is most likely that this process occurs in SNe II (Thielemann et al. 2011). The ratio  $[\text{Y}/\text{Fe}]$  stays quite constant over the metallicity range studied here, but there is relatively large scatter. This is seen in Sculptor and the Milky Way halo stars as well. In all three populations,  $[\text{Y}/\text{Ba}]$  is seen to increase as  $[\text{Ba}/\text{Fe}]$  decreases, indicating that the  $\nu\text{p}$ -process is important in each sample.

For the last element, Zr, only rather high upper limits could be determined. Since they are well above the abundances measured in the halo, it is not possible to say whether Boötes abundances are similar to those in the halo for this element too. In the halo,  $[\text{Zr}/\text{Fe}]$  decreases as  $[\text{Fe}/\text{H}]$  decreases, but from the upper limits no trend can be found. Since Zr is produced largely by the same processes as Y, it may be reasonable to assume that their abundances are also similar. Because of the similar pattern seen in Y and Zr for the Galactic halo stars from François et al. (2007), this assumption seems legit. If Boötes is indeed following the abundance pattern as seen in the halo, this would mean that Zr abundances stay constant for the stars studied.

### 8.2 What are the properties of primordial SNe in Boötes?

According to the Starfit tool that was developed to calculate yields of metal-free stars (Heger & Woosley, 2010, Chan et al. in prep), Boötes was enriched mostly by stars of relatively low mass,  $M \leq 28M_{\odot}$ . SNe in the halo are more often heavier and the maximum mass found here is  $60 M_{\odot}$ . For Sculptor, low mass SNe are quite often combined with higher mass ones. These results can be explained by looking at the

stellar mass and number of stars in each system. Boötes is a much smaller system than Sculptor, which in turn has fewer stars than the Galactic halo. If the number of stars increases, so does the chance that more massive stars are formed and thus the probability of having higher mass SNe is simply higher in the halo than in Boötes. It was possible to constrain the masses of SNe more by having measurements for Zn and Y. Without them, higher mass SNe would have been possible, just as seen in Sculptor.

Since Boötes was probably not enriched by massive SNe, it is interesting that Jablonka et al. (2015) suggest that ET0381 and J0081-0939 may also miss the ejecta of massive SNe. This could be even more true for Boötes, because it is less massive and would have more problems containing the ejecta. Jablonka et al. conclude this from the subsolar  $[\alpha/\text{Fe}]$  ratio in these stars, but Boötes has  $[\alpha/\text{Fe}]$  slightly above solar, so the reasoning in Jablonka et al. would not be true for Boötes. Subsolar values for  $[\alpha/\text{Fe}]$  would occur in gas that is not enriched by SN with  $M > 20 M_{\odot}$  (Jablonka et al. 2015, Tsujimoto et al. 1995). If measurements for ET0381 are given as input for Starfit, the best fit SN is indeed of low mass,  $M = 10.6 M_{\odot}$  and multiple SNe with  $M < 20 M_{\odot}$  also give good fits. The SNe that enriched ET0381 are probably of even lower mass than those in Boötes, meaning that Boötes is also missing ejecta, but less so than ET0381. The conclusion from Jablonka et al. is still true. This was derived for SNe from zero-metallicity stars, so there may be some changes if the yields from SNe with some Fe are also included. The assumption of zero-metallicity SNe is not completely off because all the stars have very low metallicities and only enrichment from these first stars may have occurred when they formed.

### 8.3 Is there a difference between chemical evolution properties in different environments?

After comparing elemental abundances and patterns, the final question is whether there is any significant change of chemical evolution properties in galaxies of different mass. It is expected that SNe Ia did not enrich Boötes, so this should be reflected in abundances of some elements, including Zn. Boötes stars are a bit more similar to stars of the Milky Way halo when looking at Zn and Y. The decrease of  $[\text{Zn}/\text{Fe}]$  in Sculptor that is not seen in Boötes. SNe Ia start to contribute at a later time than SN II and they produce a lot of Fe, but not that much Zn. If there would be a trend of decreasing  $[\text{Zn}/\text{Fe}]$  with increasing  $[\text{Fe}/\text{H}]$ , the slope would need to be very low, since the upper limit that was measured for Boo1137, the most metal-poor star in this sample, is not that much higher than the abundances measured for some of the more metal-rich stars. The imprint of SN Ia should especially be seen in  $\alpha$ -elements, three of which have been measured in G13. A decrease in  $[\alpha/\text{Fe}]$  is seen according to those authors if Boo41 and Boo119 are taken out of the sample. They also say that if Boo41 is included, this trend is no longer obvious and the stars seem to have abundances with a mean value and some scatter around that value. The last conclusion is also what seems most likely for Zn and Y. It is possible that the contribution of SN Ia is not found, because the star formation history of Boötes is very short.

The abundances of stars with  $[\text{Fe}/\text{H}] \lesssim -2.0$  in small dwarf galaxies that are not enriched by ejecta of SN Ia are no different from abundances in halo stars (Tolstoy et al. 2009), see e.g. Fig. 1 for Sculptor. Since the eight stars from Boötes are quite similar in abundances from Sculptor stars in the same metallicity range, the early star formation histories of Boötes and Sculptor have probably been similar. Signs of a slower chemical evolution can be found by looking at the knee in abundances of  $\alpha$ -elements and maybe Zn. Since this turning point indicates the onset of SNe Ia, so if these SNe would start at lower  $[\text{Fe}/\text{H}]$  in Boötes than in Sculptor, this would mean that Boötes was less enriched when SNe Ia started contributing. Decreasing abundances of  $\alpha$ -elements and Zn in the low metallicities of stars in Boötes would indicate a low star formation rate at those times (G13), but this trend is not clearly observed. The main difference between Sculptor and Boötes would be that Sculptor kept forming stars for a longer period and Boötes only had a short period of star formation.

## 9 Conclusion

VLT/UVES spectra of eight red giant stars in the ultra-faint dSph Boötes were extracted from the public data archive and analysed in this research project. The ESO pipeline for UVES-FLAMES was used for seven of the stars to get wavelength calibrated spectra. A wavelength calibrated and sky subtracted spectrum was already available for the last star, Boo1137, which was observed in UVES-slit mode.

The aim was to measure Zn, Y and Zr abundances and to compare them to abundances observed in Sculptor. For this, abundances of Fe, Mg, Zn, Y, Zr and Ba were measured using synthetic spectra that using the MARCS stellar atmosphere models and the spectral synthesis code Turbospec. G13 had previously analysed Fe, Mg and Ba among many other elements for seven stars, while Norris et al. (2010) had made a similar analysis for Boo1137. The stars are cover a range in metallicities:  $-3.72 \leq [\text{Fe}/\text{H}] \leq -2.17$ .

This analysis has found an offset in  $[\text{Fe}/\text{H}]$  with the previous work. This offset was  $-0.1$  dex when averaged over the sample. An offset was also found for  $[\text{Ba}/\text{Fe}]$ , but for this element only one line was included in this analysis with synthetic spectra, giving a larger uncertainty. The following conclusions could be made from an analysis of the spectra:

- The average abundance patterns in RGB stars in Boötes, Sculptor and the Milky Way halo are all very similar at similar  $[\text{Fe}/\text{H}]$ .
- $[\text{Zn}/\text{Fe}]$  measured in eight stars from Boötes was found to be very similar to that in Galactic halo stars and Sculptor at the same  $[\text{Fe}/\text{H}]$ . They miss the downward trend seen in Sculptor and thus, the stars in Boötes, like the Milky Way halo do not show signs of SN Ia enrichment in their Zn abundances.
- $[\text{Y}/\text{Fe}]$  is found to be constant in Boötes, with a certain amount of scatter, comparable to the Milky Way halo and Sculptor at the same  $[\text{Fe}/\text{H}]$ . This element is likely partly produced by the  $\nu\text{p}$ -process at low metallicities, which can be seen in the decreasing  $[\text{Y}/\text{Ba}]$  ratio as  $[\text{Ba}/\text{H}]$  increases.
- From the comparison of the abundance pattern of the CEMP-no star in Boötes, Boo119, with another one from Sculptor, ET0097, few conclusions could be made. More abundances are needed as Boo119 has only upper limits for three crucial elements, Zn, Y and Zr. Both stars are similar to each other for the elements that were measured, except for the difference in  $[\text{Fe}/\text{H}]$  that is also reflected in a difference in  $[\text{Ba}/\text{Fe}]$ .
- Comparison to zero-metallicity SNe models from Starfit were made. The SNe that enriched Boötes were found to be most likely of relatively low mass,  $M < 28 M_{\odot}$ . Having Zn and Y abundances in all systems helped constrain these masses. Those in Sculptor more often have masses  $\sim 35 M_{\odot}$  and the most massive SNe occurred in the halo, this is consistent with more massive systems having more massive SNe.
- The chemical enrichment history in Boötes was probably very similar to that in the Milky Way halo and in the more massive dSph Sculptor at the earliest times. Boötes has a much shorter star formation history than Sculptor and this could explain why the chemical abundance patterns could develop more in Sculptor.

Abundances measured for Zn from this work have helped to explain how the stars in Boötes are very similar to those in Sculptor and to Milky Way halo stars. Furthermore, Zn and Y were useful to constrain the masses of the zero-metallicity SNe that may have contributed to the enrichment of Boötes. Current results (Brown et al. 2014) indicate that the star formation history of Boötes was too short for SN Ia enrichment, but to be able to draw better conclusions about chemical evolution history of Boötes and how this relates to other galaxies, abundances of more stars should be measured. Stars spanning a larger range of metallicity (if they exist in Boötes) could tell us more about chemical evolution over time and larger numbers of stars may also show if there is indeed no chemical evolution trend of decreasing  $\alpha$ -elements and Zn at metallicity range observed here.

## 10 Acknowledgements

First of all I want to thank Eline for giving me an interesting project, helping me to do it step-by-step and making time to meet, despite being away a lot, you are a great supervisor! Also, thanks to Ása who helped me with the synthetic spectra and whom I could always mail if I had questions. Of course, thanks to all the people in the student room for random chats but also for helping with general problems. Especially thanks to Anke for being a friend as well as a fellow student.

I want to thank the computer group for helping with computer problems and giving me a better computer and the people from the secretariat for talking to us and listening to us about the reorganisation of the student room. Finally, thanks to Michael for helping me and just being there. Yes, you deserve a place in the acknowledgements ;)

## References

- Alam, S., Albareti, F. D., Allende Prieto, C. et al. (2015) *ApJSS*, 219, 12
- Alvarez, R., Plez, B. (1998) *A&A*, 330, 1109
- Andrievsky, S. M., Spite, M., Korotin, S. A., Spite, F., Bonifacio, P., Cayrel, R., François, P., Hill, V. (2010) *A&A*, 509, A88
- Asplund, M., Grevesse, N., Sauval, J. A., Scott, P. (2009) *ARA&A*, 47, 481
- Barbuy, B., Friaça, A. C. S., da Silveira, C. R., Hill, V., Zoccali, M., Minniti, D., Renzini, A., Ortolani, S., Gómez, A. (2015) *A&A*, 580, A40
- Battaglia, G., Helmi, A., Tolstoy, E., Irwin, M., Hill, V., Jablonka, P. (2008) *ApJ*, 681, L13
- Beers, T., Christlieb, N. (2005) *ARA&A*, 43, 531
- Belokurov, V., Zucker, D. B., Evans, N. W. et al. (2006) *ApJ*, 647, L111
- Belokurov, V., Zucker, D. B., Evans, N. W. et al (2007) *ApJ*, 654, 897
- Bensby, T., Feltzing, S., Oey, M. S. (2014) *A&A*, 562, A71
- Brown, Thomas M.; Tumlinson, J., Geha, M. et al. (2014) *ApJ*, 796, 91
- Burbidge, M., Burbidge, G., Fowler, W., Hoyle, F. (1957) *Reviews of Modern Physics*, 29, 547
- Busso, M., Gallino, R., Wasserburg, G. J. (1999) *ARA&A*, 37, 239
- Cayrel, R., Depagne, E., Spite, M., Hill, V., Spite, F., François, P., Plez, B., Beers, T., Primas, F., Andersen, J., Barbuy, B., Bonifacio, P., Molaro, P., Nordström, B. (2004) *A&A*, 416, 1117
- Carollo, D., Beers, T. C., Lee, Y. S. et al. (2007) *Nature*, 450, 1020
- de Boer, T. J. L., Tolstoy, E., Hill, V., Saha, A., Olsen, K., Starkenburg, E., Lemasle, B., Irwin, M. J., Battaglia, G. (2012) *A&A*, 539, A103
- Dekker, H., D'Odorico, S., Kaufer, A., Delabre, B., Kotzlowski, H. (2000) *SPIE*, 4008, 534
- Eggen, O. J., Lynden-Bell, D., Sandage, A. R. (1962) *ApJ*, 139, 748
- Fenner, Y., Prochaska, J. X., Gibson, B. K. (2004) *ApJ*, 606, 116
- François, P., Depagne, E., Hill, V., Spite, M., Spite, F., Plez, B., Beers, T. C., Andersen, J., James, G., Barbuy, B., Cayrel, R., Bonifacio, P., Molaro, P., Nordström, B., Primas, F. (2007) *ApJ*, 476, 935
- Gallino, R., Arlandini, C., Busso, M., Lugaro, M., Travaglio, C., Straniero, O., Chieffi, A., Limongi, M. (1998) *ApJ*, 497, 388
- Geisler, D., Smith, V. V., Wallerstein, G., Gonzalez, G., Charbonnel, C. (2005) *ApJ*, 129, 1428
- Gilmore, G., Norris, J. E., Monace, L., Yong, D., Wyse, R. F. G., Geisler, D. (2013) *ApJ*, 763, 61
- Gustafsson, B., Bell, R. A., Eriksson, K., Nordlund, A. (1975) *A & A*, 42, 407
- Gustafsson, B., Edvardsson B., Eriksson K., Jørgensen U.G., Nordlund Å, Plez B. (2008), *A&A*, 486, 951
- Hauschildt, P. H., Allard, F., Barman, T. et al. (2002), in *Galactic Structure, Stars and the Interstellar Medium*, ed. C. Woodward, M. Bica, & J. Shull (ASP: San Francisco), 427
- Heger, A., Woosley, S. E. (2002) *ApJ*, 567, 532
- Heger, A., Woosley, S. E. (2010) *ApJ*, 724, 341
- Ishigaki, M. N., Aoki, W., Chiba, M. (2013) *ApJ*, 771, 67
- Jablonka, P., North, P., Mashonkina, L., Hill, V., Revaz, Y., Shetrone, M., Starkenburg, E., Irwin, M., Tolstoy, E., Battaglia, G., Venn, K., Helmi, A., Primas, F., François, P. (2015), *A&A*, 583, A67
- Koposov, S. E., Gilmore, G., Walker, M. G. et al. (2011) *ApJ*, 736, 146
- Martin, N. F., Ibata, R. A., Chapman, S. C., Irwin, M., Lewis, G. F. (2007) *MNRAS*, 380, 281
- Modigliani, A., Larsen, J.M. (2015), *UVES Pipeline User Manual*, VLT-MAN-ESO-19500-3016, Issue 18.4
- Muñoz, R. R., Carlin, J. L., Frinchaboy, P. M., Nidever, D. L., Majewski, S. R., Patterson, R. J. (2006) *ApJ*, 650, L51
- Nissen, P. E., Schuster, W. J. (2011) *A & A* 530, A15
- Norris, J. E., Yong, D., Bessel, M. S., Christlieb, N., Asplund, M., Gilmore, G., Wyse, R. F. G., Beers, T. C.; Barklem, P. S., Frebel, A., Ryan, S. G. (2013) *ApJ*, 762, 28
- Norris, J. E., Yong, D., Gilmore, G., Wyse, R. F. G. (2010) *ApJ*, 711, 350
- Pasquini, L., Avila, G., Blecha, A. et al. (2002) *The Messenger*, 110, 1
- Piskunov, N. E., Kupka, F., Ryabchikova, T. A., Weiss, W. W., & Jeffery, C. S. (1995) *A&A Supplement*, 112, 525

- Plez, B. (2012) Astrophysics Source Code Library, record ascl:1205.004
- Reddy, B. E., Lambert, D. L., Allende Prieto, C. (2006) MNRAS, 367, 1329
- Reddy, B. E., Tomkin, J., Lambert, D. L., Allende Prieto, C. (2003) MNRAS, 340, 304
- Sbordone, L., Bonifacio, P., Buonanno, R., Marconi, G., Monaco, L., Zaggia, S. (2007) A&A, 465, 815
- Searle, L., Zinn, R. (1978) ApJ, 225, 357
- Shetrone, Matthew D.; Côté, P., Sargent, W. L. W. (2001) ApJ, 548, 592
- Shetrone, M., Venn, K. A., Tolstoy, E., Primas, F., Hill, V., Kaufer, A., (2003) ApJ, 125, 684
- Siegel, M. H. (2006) ApJ, 649, L83
- Sparke, L. S., Gallagher, J. S. (2007) Galaxies in the Universe: An Introduction, Cambridge University Press, second edition
- Springel, V., White, S. D. M., Jenkins, A., et al. (2005) Nature, 435, 629
- Simon, J. D., Jacobson, H. R., Frebel, A., Thompson, I. B., Adams, J. J., Shetrone, S. A. (2015) ApJ, 802, 93
- Skúladóttir, Á., Tolstoy, E., Salvadori, S., Hill, V., Pettini, M., Shetrone, M. D., Starkenburg, E. (2015) A&A, 574, A129
- Skúladóttir, Á. et al. (2016) *Sulphur, Zinc and Carbon in the Sculptor Dwarf Spheroidal Galaxy*, PhD thesis, Rijksuniversiteit Groningen
- Starkenburg, E., Hill, V., Tolstoy, E., François, P., Irwin, M. J., Boschman, L., Venn, K. A., de Boer, T. J. L., Lemasle, B., Jablonka, P., Battaglia, G., Groot, P., Kaper, L. (2013) A&A, 549, 88
- Tafelmeyer, M., Jablonka, P., Hill, V., et al. (2010) A&A, 524, 58
- Thielemann, F.-K., Arcones, A., Käppeli, R., et al. (2011) Progress in Particle and Nuclear Physics, 66, 346
- Tolstoy, E., Irwin, M. J., Helmi, A., Battaglia, G., Jablonka, P., Hill, V., Venn, K. A., Shetrone, M. D., Letarte, B., Cole, A. A., Primas, F., François, P., Arimoto, N., Sadakane, K., Kaufer, A., Szeifert, T., Abel, T. (2004) ApJ, 617, L119
- Tolstoy, E., Hill, V., Tosi, M. (2009) ARA&A, 47, 371
- Tolstoy, E., Venn, K. A., Shetrone, M., Primas, F., Hill, V., Kaufer, A., Szeifert, T. (2003) ApJ, 125, 707
- Travaglio, C., Gallino, R., Arnone, E., Cowan, J., Jordan, F., Sneden, C. (2004) ApJ, 601, 864
- Tsujimoto, T., Nomoto, K., Yoshii, Y., Hashimoto, M., Yanagida, S., Thielemann, F.-K. (1995) MNRAS, 277, 945
- Umeda, H., Nomoto, K. (2002) ApJ, 565, 385
- Venn, K. A., Shetrone, M. D., Irwin, M. J., Hill, V., Jablonka, P., Tolstoy, E., Lemasle, B., Divell, M., Starkenburg, E., Letarte, B., Baldner, C., Battaglia, G., Helmi, A., Kaufer, A., Primas, F. (2012) ApJ, 751, 102
- Weaver, T. A., Zimmerman, G. B., Woosley, S. E., (1978) ApJ, 228, 1021
- White, S. D. M., Rees, M. J. (1978) MNRAS, 183, 341
- Willman, B., Dalcanton, J. J., Martinez-Delgado, D. et al. (2005) ApJ, 626, L85
- Wolf, J., Martinez, G. D., Bullock, J. S., Kaplinghat, M., Geha, M., Muñoz, R. R., Simon, J. D., Avedo, F. F. (2010) MNRAS, 406, 1220
- Woosley, S. E., Heger, A., Weaver, T. A. (2002) Reviews of Modern Physics, 74, 1015
- Yong, D., Norris, J. E., Bessell, M. S., Christlieb, N., Asplund, M., Beers, T. C., Barklem, P. S., Frebel, A., Ryan, S. G. (2013) ApJ, 762, 26
- York, D. G. et al. (2000) AJ, 120, 1579
- Zucker D. B. et al. (2006a) ApJ, 643, L103
- Zucker D. B. et al. (2006b) ApJ, 650, L41

[http://www.astropa.unipa.it/Telescopi\\_Ottici/VLT/FLAMES.gif](http://www.astropa.unipa.it/Telescopi_Ottici/VLT/FLAMES.gif), retrieved on 14-06-2016

# Appendices

## A Linelist

Element	Wavelength (Ångström)
Mg I	5172.68
Mg I	5183.60
Mg I	5528.41
Fe I	4871.32
Fe I	4872.14
Fe I	4891.49
Fe I	4918.99
Fe I	4920.50
Fe I	4938.81
Fe I	4939.69
Fe I	4994.13
Fe I	5001.87
Fe I	5006.12
Fe I	5049.82
Fe I	5051.63
Fe I	5068.77
Fe I	5074.75
Fe I	5079.74
Fe I	5083.34
Fe I	5123.72
Fe I	5127.36
Fe I	5150.84
Fe I	5151.91
Fe I	5162.27
Fe I	5166.28
Fe I	5171.60
Fe I	5191.46
Fe I	5192.34
Fe I	5194.94
Fe I	5216.27
Fe I	5225.53
Fe I	5232.94
Fe I	5254.96
Fe I	5266.56
Fe I	5281.79
Fe I	5283.62
Fe I	5302.31
Fe I	5307.36
Fe I	5324.18
Fe I	5328.04
Fe I	5328.53
Fe I	5339.93
Fe I	5369.97
Fe I	5371.49
Fe I	5383.38
Fe I	5393.18
Fe I	5397.13
Fe I	5405.77
Fe I	5429.70

---

Element	Wavelength (Ångström)
Fe I	5434.52
Fe I	5446.92
Fe I	5455.61
Fe I	5497.52
Fe I	5501.46
Fe I	5506.78
Fe I	5569.62
Fe I	5572.84
Fe I	5586.76
Fe I	5615.64
Mg I	5172.684
Mg I	5183.604
Mg I	5528.405
Zn I	4810.53
Y II	4854.86
Y II	4883.684
Y II	5087.416
Zr II	5112.27
Zr II	5372.47
Zr II	5418.02
Zr II	5477.82
Ba II	4934.08

---